Unraveling the Internal Magnetic Field Structure of the Earth-directed Interplanetary Coronal Mass Ejections During 1995 – 2015

Teresa Nieves-Chinchilla[1,2] (ID) · **Lan K. Jian[1]** (ID) ·
Laura Balmaceda[1,3] (ID) · **Angelos Vourlidas[4]** (ID) ·
Luiz F. G. dos Santos[1,2] (ID) · **Adam Szabo[1]** (ID)

Abstract The magnetic field configurations associated with interplanetary coronal mass ejections (ICMEs) are the *in situ* manifestations of the entrained magnetic structure associated with coronal mass ejections (CMEs). We present a comprehensive study of the internal magnetic field configurations of ICMEs observed at 1 AU by the *Wind* mission during 1995 – 2015. The goal is to unravel the internal magnetic structure associated with the ICMEs and establish the signatures that validate a flux-rope structure. We examine the expected magnetic field signatures by simulating spacecraft trajectories within a simple flux rope, *i.e.*, with circular–cylindrical (CC) helical magnetic field geometry. By comparing the synthetic configurations with the 353 ICME *in situ* observations, we find that only 152 events (F_r) display the clear signatures of an expected axial-symmetric flux rope. Two more populations exhibit possible signatures of flux rope; 58 cases (F^-) display a small rotation ($< 90°$) of the

✉ T. Nieves-Chinchilla
Teresa.Nieves@nasa.gov

L.K. Jian
lan.jian@nasa.gov

L. Balmaceda
Laura.Balmaceda@nasa.gov

A. Vourlidas
angelos.vourlidas@jhuapl.edu

L.F.G. dos Santos
luizfernando.guedesdossantos@nasa.gov

A. Szabo
adam.szabo-1@nasa.gov

[1] Heliophysics Science Division, NASA Goddard Space Flight Center, Greenbelt, MD, USA

[2] Physics Department, The Catholic University of America, Washington, DC, USA

[3] George Mason University, Arlington, VA, USA

[4] Applied Physics Laboratory, Johns Hopkins University, Laurel, MD, USA

magnetic field direction, interpreted as a large separation of the spacecraft from the center, and, 62 cases (F^+) exhibit larger rotations, possibly arising from more complex configuration. The categories, C_x (14%) and E events (9%), reveal signatures of complexity possibly related with evolutionary processes. We then reconstruct the flux ropes assuming CC geometry. We examine the orientation and geometrical properties during the solar activity levels at the end of Solar Cycle 22 (SC22), SC23 and part of SC24. The orientation exhibits solar cycle trends and follow the heliospheric current sheet orientation. We confirm previous studies that found a Hale cycle dependence of the poloidal field reversal. By comparing our results with the occurrence of CMEs with large angular width (AW > 60°) we find a broad correlation suggesting that such events are highly inclined CMEs. The solar cycle distribution of bipolar *vs.* unipolar B_z configuration confirms that the CMEs may remove solar cycle magnetic field and helicity.

Keywords Coronal mass ejections, interplanetary · Solar cycle, observations · Solar wind disturbances

1. Introduction

The interplanetary counterparts of coronal mass ejections (ICMEs) are the main drivers of geomagnetic activity. In addition to transporting large amount of mass and magnetic flux away from the Sun, their internal magnetic field structure is prone to be coupled to the upper magnetosphere triggering magnetic reconnection processes that allow the injection of solar magnetic energy into the whole magnetospheric system. Thus, the reliable prediction of the ICME internal magnetic field structure is a requisite for developing a robust space weather forecast capability.

A breakthrough in the understanding of the ICME internal structure was reached by Burlaga *et al.* (1981), Klein and Burlaga (1982) with the magnetic-cloud (MC) concept. Under this definition, the authors interpreted the *in situ* observations as a 3D magnetic flux-rope topology confining cold plasma, *i.e.*, increase of the magnetic field, smooth rotation in the magnetic field direction and low proton temperature. The obvious next steps were to implement known plasma physics flux-rope models (Lundquist, 1950, for instance) to techniques (Lepping, Burlaga, and Jones, 1990) to reconstruct the internal ICME magnetic configuration as observed by the magnetometers onboard satellites and to provide valuable information about the orientation, geometry, and other magnetic parameters, such as the central magnetic field, magnetic flux or chirality. Ever since, ICMEs with smooth and monotonic internal magnetic field changes have been systematically labeled MCs, irrespective of whether the *in situ* measurements fulfilled all the MC definition or not.

MCs are not always detected within ICMEs (see Richardson and Cane, 2004) despite the fact that flux ropes are always expected based on the CME eruption theories (see Vourlidas, 2014, and the references therein). This might result from changes during IP evolution (see Manchester *et al.*, 2017, and the references therein), from spacecraft crossing far from the ICME core, or possibly from the topological complexity of the magnetic structure during CME initiation in the solar corona. In any case, our information about ICME internal magnetic structure is limited by a single spacecraft crossing through the large structure that leaves a considerable amount of uncertainty. This practical observational constraint is used to justify the application of flux-rope models to *in situ* reconstructions even when the measurements do not display the expected signatures of a flux-rope crossing.

To explain these partial flux-rope signatures, Nieves-Chinchilla *et al.* (2018) extended the MC definition by introducing the concept of the magnetic obstacle (MO) and compil-

ing a catalog of MO-ICMEs observed by *Wind* in the period 1995 – 2015. MOs are not always characterized by a full single rotation or even a rotation, and they, therefore, cannot be fully described by the MC flux-rope configuration. These MO configurations have been variously called "magnetic-cloud-like", "flux-rope-like" or "non-classic-MC" (see *e.g.* Lepping, Wu, and Berdichevsky, 2005; Wu and Lepping, 2015; Gopalswamy *et al.*, 2015; Badruddin, Mustajab, and Derouich, 2018). The common thread is that these structures are reconstructed using flux-rope topologies. However, we understand that this approach may result in confusion rather than shed light into the magnetic nature of CME and that it is necessary to explore what are the limitations in such scenarios.

   This is the motivation behind this paper. Inspired by the findings in Nieves-Chinchilla *et al.* (2018), we want to understand in depth what *in situ* magnetic field observations should be expected when a spacecraft crosses a flux rope with different trajectories. The paper comprises two parts. In the first part, we simulate the expected magnetic field signatures for a spacecraft crossing a large magnetic flux-rope structure under all possible trajectories. We then compile a guide to properly identify the magnetic flux-rope observations associated with ICMEs (Section 2). We employ the simplest geometry, *i.e.*, the circular–cylindrical geometry based on the Nieves-Chinchilla *et al.* (2016) model and reconstruction techniques. By using different flux-rope orientations and impact parameters, we evaluate the effects on the *in situ* observations. This exercise helps us identify flux ropes in the actual observations. Thus, such events can be classified accordingly as flux ropes amenable to reconstruction, or not flux ropes that require a different analysis method (Section 3).

   In Section 4, we report the output from the reconstructions solely for events displaying flux-rope signatures. The analysis extends from the end of Solar Cycle 22 (SC22), through Cycle 23 (SC23), to the maximum of Cycle 24 (SC24). Section 5 gives the summary and conclusions.

2. Simulation of Virtual Spacecraft Crossing an Axial-symmetric Flux Rope

The circular–cylindrical analytical flux-rope model (henceforth the CC model) was presented in Nieves-Chinchilla *et al.* (2016). The flux-rope magnetic topology was established as an axially symmetric magnetic field cylinder with a twisted magnetic field. The magnetic field components in the circular–cylindrical coordinate system are

$$B_r = 0,$$
$$B_y = B_y^0 \left[1 - \left(\frac{r}{R} \right)^2 \right], \tag{1}$$
$$B_\varphi = -H \frac{B_y^0}{|C_{10}|} \left(\frac{r}{R} \right),$$

where the two direct output parameters are B_y^0, the magnetic field at the center of the flux rope and C_{10} a measure of the force-freeness with the H sign ($+1$ or -1) that indicates if the flux rope is right- or left-handed. The radius of the flux-rope cross-section, R, is a derived parameter (see Equation 5 in Hidalgo *et al.*, 2002) and r is the radial distance that describe the spacecraft trajectory.

   These equations summarize the model that describe physically the characteristics of heliospheric flux ropes by assuming a geometry with axial symmetry and circular cross-section. The reconstruction technique has been largely discussed by Nieves-Chinchilla *et al.*
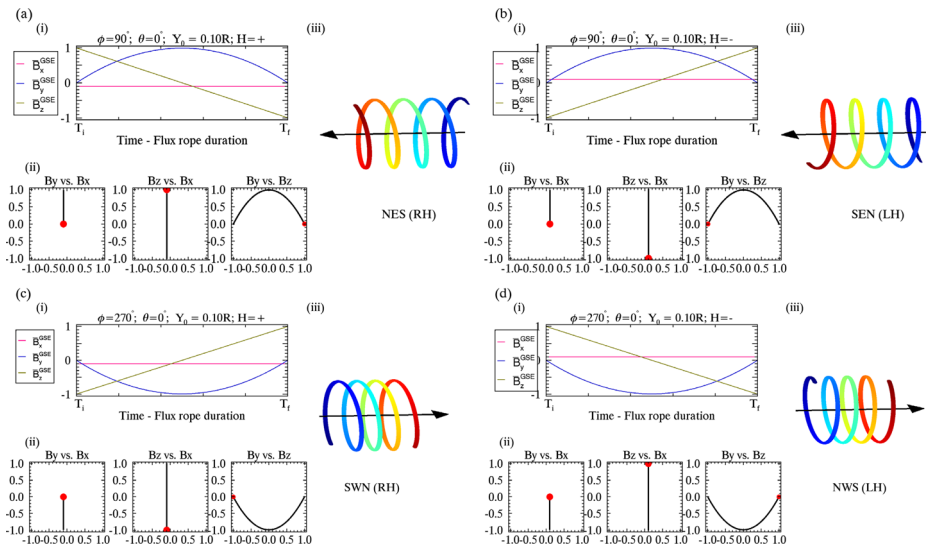
Figure 1 (**a**) *In situ* signatures in the GSE coordinate system and sketch representing the north-east-south, right-handed (NES-RH), (**b**) representing the south-east-north, left-handed (SEN-LH), (**c**) south-west-north, right-handed (SWN-RH), and (**d**) north-west-south, left-handed (NWS-LH). For each configuration is included: (**i**) Temporal variation, (**ii**) magnetic hodograms of the GSE magnetic components, and (**iii**) flux-rope configuration sketch.

(2016), Nieves-Chinchilla (2018). The trajectory of the spacecraft is inferred by using the minimization of the χ^2 function (equation 13 in Nieves-Chinchilla, 2018) and therefore the orientation of the flux rope. Thus, in addition to the model parameters (B_y^0, C_{10}), the longitude (ϕ), the tilt (θ) and impact parameter (y_0) complete the five direct output parameters.

In this section we will simulate different flux-rope axis orientations, or spacecraft trajectories, and return the expected synthetic magnetic field observations. In these simulations, we fix the flux-rope radius, $R = 0.07$ AU, and the flux-rope bulk velocity to $v_{sw} = 450$ km s^{-1}. The transit time (duration) of the spacecraft within the structure can be obtained from Equations 2 and 5 in Hidalgo *et al.* (2002). Thus,

$$t_s = \frac{2}{v_{sw}\sqrt{1 - \sin^2\phi\cos^2\theta}}\sqrt{R^2 - y_0^2}. \tag{2}$$

2.1. Synthetic Magnetic Field Configurations

One of the first studies devoted to exploring flux-rope configurations was carried out by Bothmer and Schwenn (1998). In this study, the authors first classified the ICME internal configuration in terms of a magnetic quasi-cylindrical geometry, with left- (LH) or, right-handed (RH) chirality, and with the axis laying in the ecliptic plane, *i.e.*, with very low inclination. Figure 1 shows synthetic solar wind data of a magnetometer onboard a virtual spacecraft flying through a flux-rope cylinder for four low inclined magnetic field configurations in GSE (geocentric solar ecliptic) coordinate system ($\phi = 90°, 270°, \theta = 0°$ with left/right chirality). The configurations correspond to the leading and trailing magnetic field polarities or chirality, *i.e.*, right-handed (RH, $+$) or left-handed (LH, $-$), and to the axis eastwards (E, $\phi = 90°$) or westwards (W, $\phi = 270°$). In the simulation, the magnetic field

has been normalized to the central magnetic field, B_y^0 and $|C_{10}| = 1$. In the north-to-south (NS) configurations, the B_z^{GSE}-component goes from positive to negative (Figure 1a, 1d) and vice versa for the south-to-north (SN) configurations (Figure 1b, 1c). Thus, Figure 1 is organized as the eastwards flux tubes with both polarities (a) NES-RH and (b) SEN-LH, and the westwards combined with both polarities in the (c) SWN-RH and (d) NWS-LH. Each combination includes (i) the expected temporal variation of the *in situ* magnetic field components in GSE coordinate system, (ii) the magnetic hodograms, and, (iii) the figure included the corresponding magnetic field sketch.

The temporal variation of the magnetic field components (i) is within the time of the spacecraft crossing the structure, where T_i is the first encounter of the spacecraft with the flux rope and T_f is the last contact of the spacecraft. Then $T_f - T_i$ is the duration of the magnetic cloud (Equation 2). For these simulations, we have selected a very small impact parameter (small distance of the spacecraft to the flux-rope center) $y_0 = 0.10R$, where R is the radius of the tube cross-section. This configuration was named bipolar by Mulligan, Russell, and Luhmann (1998) because of the double sign in the B_z-component. The y-component is aligned with the GSE-y-axis and therefore is positive (E, Figure 1a, 1b) or negative (W, Figure 1c, 1d), and maximum at the center. Finally, the x-component is close to zero since the spacecraft is crossing close to the tube center (y_0 small). The hodograms, bottom three square plots (iii), are built by combining two magnetic field components, B_j^{GSE}, with $j = (x, y, z)$. In each square plot, T_i is indicated with a red dot. In each figure, from Figure 1a to 1d, there is a full (180°) rotation in the combined plot of B_y^{GSE} *vs.* B_z^{GSE}.

Mulligan, Russell, and Luhmann (1998) also added four more categories (and named them unipolar since B_z does not change sign, either positive or negative) for the flux-rope configurations that can be visualized as a highly inclined cylinder with the axis perpendicular to the ecliptic plane. In Figure 2 these four categories are shown using the same convention as Figure 1. Thus, the B_z^{GSE} component is aligned with the local B_z component and does not change sign, *i.e.*, northwards or southwards and with the maximum at the center. In Figure 2a, 2b, B_z is northwards with the two combined chirality (RH and LH), and in Figure 2c, 2d is southwards with the two combined chiralities (RH and LH). In these four scenarios the orientation is $\phi = 90°$ but the tilt (θ) is 90° for the northwards configuration and $-90°$ for the southwards configuration. Note that the configuration would be the same for any ϕ combined with $\theta \approx [\pm]90°$.

For highly-inclined flux tubes, the magnetic field component profiles B_y^{GSE} and B_z^{GSE} are swapped compared to the low-tilted tubes. In this case, the rotation is clearly exhibited in the y-component and the z-component remains positive or negative with the maximum value at the tube center. The east-to-west configurations are the ENW-LH and ESW-RH (Figure 2b, 2c). The B_z^{GSE} component remains positive for the northwards (N) configuration (Figure 2a, 2b) and negative for the southwards (S) configurations (Figure 2c, 2d). The B_x^{GSE} component remains constant for all configuration as discussed in Figure 1. Again, the rotation is clearly depicted in the hodograms (ii), where the case B_y^{GSE} *vs.* B_z^{GSE} exhibits the full 180° rotation.

In real observations, we cannot force the flux ropes to reach the spacecraft with a high ($|\theta| > 60°$) or low ($|\theta| < 30°$) inclined tilt; with the tube axis completely perpendicular to the Sun–Earth line ($\phi \approx 90°$ or $\approx 270°$); or, with the impact parameter close to the tube axis ($y_0 < 0.10R$). Traditionally, the threshold between unipolar or bipolar magnetic configurations has been located around $\theta = 45°$ (Huttunen *et al.*, 2005) and called Intermediate by Palmerio *et al.* (2018) but there is not a study to evaluate the impact of the longitude (ϕ) in the configuration.

Figure 3 includes the synthetic data for magnetic configurations with a more realistic longitude, tilt, and impact parameter. Figure 3a shows the case with $(\phi, \theta, y_0) =$
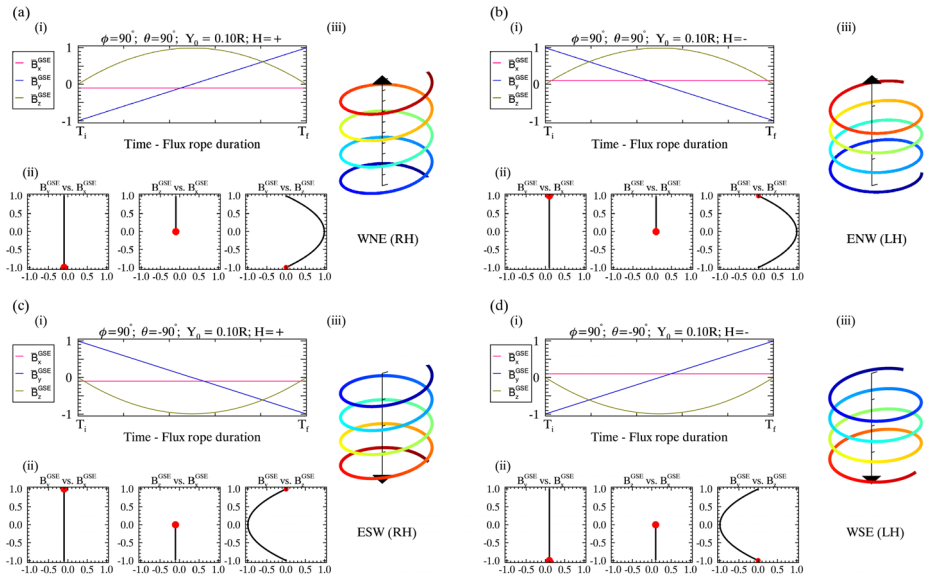
Figure 2 (**a**) *In situ* signatures in the GSE coordinate system and sketch representing the west-north-east, right-handed (WNE-RH), (**b**) representing the east-north-west, left-handed (ENW-LH), (**c**) east-south-west, right-handed (ESW-RH), and (**d**) west-south-east, left-handed (WSE-LH). For each configuration is included: (**i**) Temporal variation, (**ii**) magnetic hodograms of the GSE magnetic components, and (**iii**) flux-rope configuration sketch.
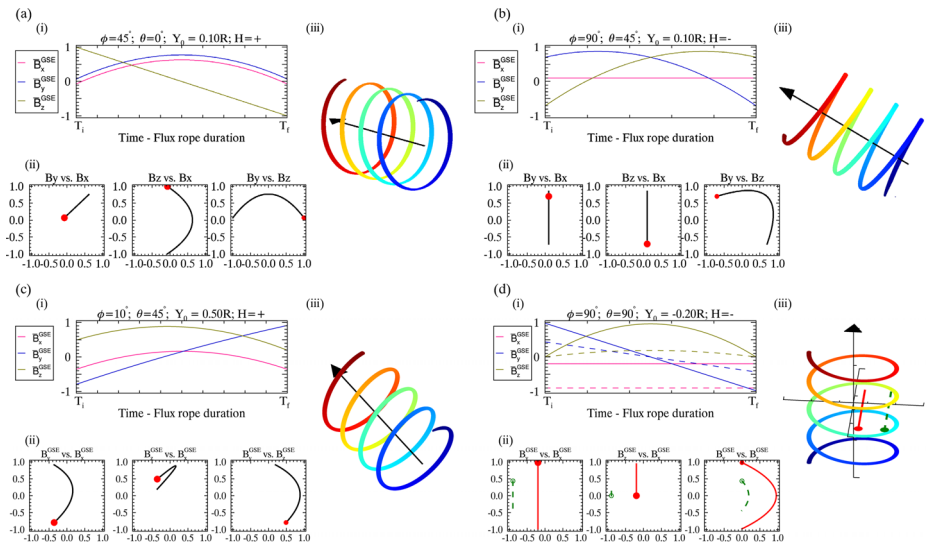
Figure 3 *In situ* signatures in the GSE coordinate system and sketch representing a combination of ϕ and θ angles. (**a**) $\phi = 45°$ and $\theta = 0°$, right-handed, (**b**) $\phi = 90°$ and $\theta = 45°$, left-handed, (**c**) $\phi = 10°$ and $\theta = 45°$, right-handed, and (**d**) $\phi = 90°$ and $\theta = 90°$, left-handed. This last figure include two spacecraft impact parameter, $y_0 = 0.2$ (*red*), and $y_0 = 0.8$ (*green*). For each configuration is included: (**i**) Temporal variation, (**ii**) magnetic hodograms of the GSE magnetic components, and (**iii**) flux-rope configuration sketch.

$[45°, 0°, 0.10R]$. In this case, the B_z^{GSE} component maintains the bipolarity but the B_y^{GSE} component is not aligned with the flux-rope axis and B_x^{GSE} component will also be curved. In general, while the flux-rope axis remains in the ecliptic plane, we would still expect a complete rotation in this component if the spacecraft crosses completely the flux-rope cross-section side to side.

Figure 3b depicts a longitude angle of $\phi = 90°$ and a mid axis inclination of $\theta = 45°$. In this configuration the B_z^{GSE} displays bipolarity as well as the B_y^{GSE} component. This config-uration shows a hybrid magnetic field profile between the previously described bipolar and unipolar configurations. In Figure 3c, the magnetic configuration changes with the same tilt but longitude more aligned with the Sun–Earth line ($\phi = 10°$) and higher impact parameter ($y_0 = 0.50R$) exhibits unipolar B_z.

For completeness, we have included a series of plots in the Appendix, Figure 14 with B_x^{GSE} (red), B_y^{GSE} (blue) and B_z^{GSE} (green) profiles, to serve as a guide of the different flux-rope orientations. Each plot fixes the ϕ, y_0 and chirality and provides the component profiles for $\theta = [0°, 30°, 60°, 90°]$, where the line-thickness from higher to lower indicate lower tilt to higher tilt. From this figure, the reader can use Figures 1, 2 and 3 to estimate the expected magnetic signatures of different axis orientations by changing the orientation from north to south, east to west, or the chirality as discussed previously.

The configuration in Figure 3c illustrates the effect of the combination θ and ϕ with an impact parameter of $y_0 = 0.50R$. In this case, the rotation is displayed in, at least, two of the three hodograms. Due to the combination of the orientation and the increasing in the impact parameter, the rotation measured in the hodograms is less than $180°$. This configuration is a transition between Figure 14a and Figure 3a.

Figure 3d also illustrates the effect of the separation of the spacecraft from the flux-rope axis. The orientation is aligned with the Sun–Earth line and had maximum tilt. Two different impact parameters are illustrated. The red dashed line (the dot indicates the start time) on the sketch is $y_0 = 0.20R$ with red lines in the hodograms and colored solid line in the temporal plot. The configuration with a high impact parameter, $y_0 = 0.80R$, is displayed with green dashed line in the sketch, green line on the hodograms and dashed colored line in the temporal plot. The separation of the spacecraft affects the magnetic field configuration of the temporal plot with a separation of the B_x^{GSE} component from the zero level, flattening in the B_z^{GSE} component and a lower slope in the B_y^{GSE} component.

Figure 15 exhibits two more scenarios. In the top figures, (a) and (b), the flux-rope axis is almost perpendicular to the Sun–Earth line ($\phi = 90°$) and highly inclined ($\theta = 90°$) but two impact parameters to evaluate the effect of the increase in the impact parameter. In this case, there is a change in the B_y^{GSE} slope, the B_z^{GSE} curvature and increase of the B_x^{GSE} distance to the 0-level as the y_0 increases (Démoulin, Dasso, and Janvier, 2013). In the bottom two cases, (c) – (d) for the same longitude and impact parameter, display the effect of the change from low longitude ($\phi = 30°$) higher latitude ($\phi = 60°$). During this range of transition from B_z^{GSE} bipolar to unipolar and B_y^{GSE} unipolar to bipolar, both component are partially bipolar with more o less emphasis in each polarity as the inclination changes. Thus, during this interval, the configuration displays a hybrid combination of polarity in the magnetic field components.

2.2. Threshold Between Bipolarity and Unipolar B_z Configuration

One of the ultimate outcomes that this study provides is the range of angle combinations of the geometrical parameter that will display a bipolar B_z configurations. As discussed previ-ously, the tilt (θ) is not the only angle to take into consideration but the axis longitude, ϕ,
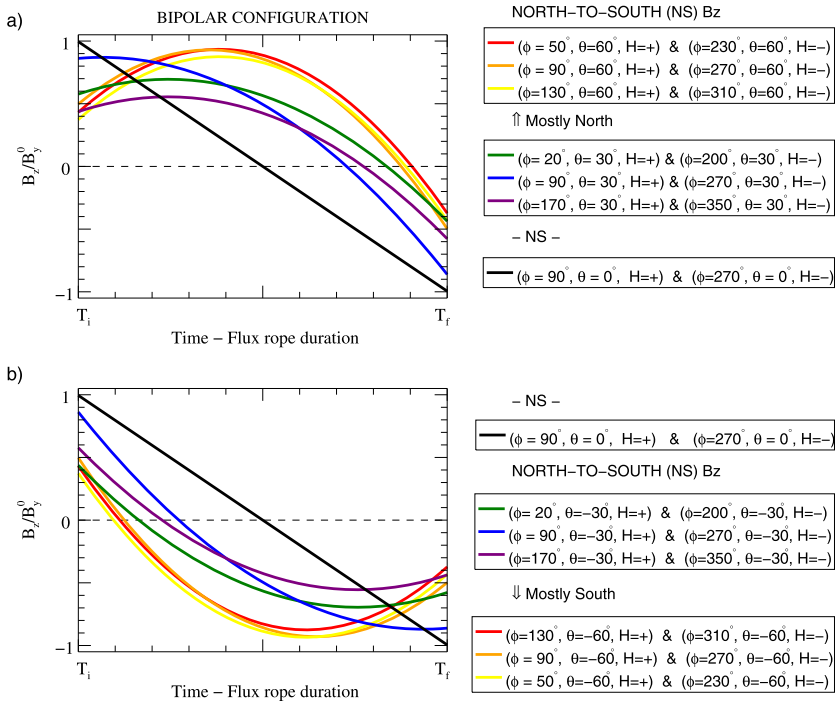
Figure 4 Combination of flux-rope axis configurations; longitude (ϕ), tilt (θ), and chirality (H) fixing the impact parameter, $Y_0 = 0.10R$, to obtain a bipolar B_z configuration normalized to the central magnetic field, B_y^0.

also play a role. Figure 4 explores different ϕ, θ and chirality combinations and aids to determine different ranges or intervals for the NS configuration in the GSE coordinate system. Note that the discussion above, in Section 2.1 and later in this section, can be applied to the case of RTN (Radial Tangential Normal) coordinate system just taking into account that $\phi_{\mathrm{GSE}} = \phi_{\mathrm{RTN}} + 180°$. Thus, for the axis perpendicular to the Sun–Earth line, with $\phi_{\mathrm{GSE}} = 90°$ or 270°, is switched to $\phi_{\mathrm{RTN}} = 270°$ or 90°, and the $\phi_{\mathrm{GSE}} = 0°$, pointed from the observer to the Sun, is $\phi_{\mathrm{RTN}} = 180°$.

Figure 4a displays the profiles ($\theta > 0°$) of northwards tilts with the central magnetic field pointing eastwards ($\phi < 180°$) with positive chirality or westwards ($\phi > 180°$) with negative chirality. Figure 4b display the profiles of southwards tilts ($\theta < 0°$) with the central magnetic field pointing eastwards ($\phi < 180°$) with positive chirality or westwards ($\phi > 180°$) with negative chirality. Note that the B_z^{GSE} profile coincides with certain eastwards or westwards angle-chirality combinations. Thus, for instance, in the boundary between northwards or southwards, with $\theta = 0°$ (black line in both figures), $\phi = 90°$ with positive chirality is eastwards and $\phi = 270°$ with negative chirality is westwards. Note that, in these cases, eastwards or westwards will determine the B_y^{GSE} sign (see Figures 14 for illustrations). By changing the chirality in the set of combinations included in the figure, the configuration switches from NS to SN.

Following the definitions given by Lepping *et al.* (2015) we have considered the cases called mostly north (mostly-N) or mostly south (mostly-S). These cases will be called here as hybrid since they are in the transition between highly ($\theta > |60|°$) and lowly ($\theta < |30|°$)

Table 1 Ranking the polarity.

Name	Description	Portions of polarity
N	north	N[90 – 100]%, S[10 – 0]%
NSN	NS mostly N	N[70 – 90]%, S[30 – 10]%
NS	north-to-south	N[30 – 70]%, S[70 – 30]%
NSS	NS mostly S	N[10 – 30]%, S[90 – 70]%
S	south	N[0 – 10]%, S[100 – 90]%
S	south	S[90 – 100]%, N[10 – 0]%
SNS	SN mostly S	S[70 – 90]%, N[30 – 10]%
SN	south-to-north	S[30 – 70]%, N[70 – 30]%
SNN	SN mostly N	S[10 – 30]%, N[90 – 70]%
N	north	S[0 – 10]%, N[100 – 90]%

inclined axis. In Figure 4a, this transition range of mostly-N-to-NS is depicted with lines in yellow–orange–red colors ($\theta = 60°$) and purple–blue–green colors ($\theta = 30°$). Note that we have included for each tilt three lines that define the range of longitudes (ϕ). Thus, for the highly inclined cases, the longitude angle goes from $\phi = 50°$ and $\phi = 230°$ (combinations displayed with the upper red line) to $\phi = 130°$ and $\phi = 310°$ (combinations displayed with the bottom yellow line). In between, for the cases with the axis perpendicular to the Sun–Earth line (combination represented with orange color, $\phi = 90°$, $270°$), the slope of the curve is slightly steeper. In these cases, the B_z component is $\approx 90\%$ north and the transition from N-to-S occurs in the trailing time boundary, closer to T_f. The bottom range of this transition region is defined by the combinations with $\theta = 30°$ (lines in green–blue–purple colors). Note that now the ϕ range is larger, for instance, for the eastwards combinations, as the longitude goes from $\phi = 20°$ (upper green curve) to $\phi = 170°$ (bottom purple curve). Therefore, it sweeps 60° more. The same is the case for the westwards combinations with ϕ from 200° to 350°. In these cases, the slope of the curve increases significantly when $\phi = 90°$ or $\phi = 270°$ is reached (combination in blue line).

The same discussion can be carried out for the mostly-S combinations. In these cases the again the green–blue–purple combinations define the souther NS scenarios. They are highly inclined with the central magnetic field pointing toward the south ($\theta = -60°$). The change in the polarity from N-to-S occurs in the first period of the flux-rope duration ($\approx 10\%$). The lower tilt for the mostly-S bipolar combinations are marked by the red-orange-yellow combinations. In these cases the transition occurs in the $\approx 30\%$ of the time that the spacecraft is within the flux rope. Again, the slope of the B_z curve increases as ϕ approaches the perpendicular to the Sun–Earth line.

In this discussion we have considered that the spacecraft is crossing close to the flux-rope center ($Y_0 = 0.10R$). The fact that it is crossing above or below the axis does not affect the B_z rotation only the distance of the spacecraft to the flux-rope center. Thus, as $|Y_0|$ increases the slope decreases and the maximum $|B_z^{GSE}/B_y^0|$ rate also decreases. Thus, the range for ϕ can also be affected. For completeness, we have included the similar scenarios in Figure 16 for an impact parameter of $Y_0 = 0.50R$. Note that the range for ϕ decreases in 60° for a tilt of $\theta = 30°$.

Here we have shown the expected magnetic field configurations and hodograms of the basic flux-rope magnetic configurations. Obviously, reality is more complex than flux-rope axis with high or low tilt, accordingly we have illustrated the hybrid case for discussion. We want to highlight an important outcome in this section: none of the simulated configuration

	$F\ [F_r, F^-, F^+]$	C_x	E	Total
Total	272 [152, 58, 62]	51	30	353
	77% [43%, 16%, 18%]	14%	9%	
SC23	153 [81, 32, 40]	30	25	208
	74% [39%, 15%, 19%]	14%	12%	
SC23 [short]	109 [63, 19, 27]	23	21	154
	71% [41%, 12%, 17%]	15%	14%	
SC24	102 [61, 23, 18]	20	4	126
	81% [48%, 18%, 14%]	16%	3%	

Table 2 Occurrence of events by category. The statistics include the total dataset, the Solar Cycle 23 (SC23, from June 1, 1996 to December 31, 2008) and Solar Cycle 24 (SC24, from 2009 to 2015). SC23 [short] includes the statistic of a SC23 subset data (from June 1, 1996 to May 31, 2003).

displays a rotation of more than 180°. In the next section, we will compare the synthetic data with the actual *Wind* observations in order to investigate the internal magnetic structure of ICMEs and evaluate the appropriateness of the axial-symmetric magnetic configuration to reconstruct such structures.

3. Magnetic Obstacles Observed Within ICMEs

In this section, we revisit the ICMEs observed by *Wind* in the period 1995 – 2015 and reported in Nieves-Chinchilla *et al.* (2018) to classify them according to their magnetic configuration signatures. We reconstruct only events with magnetic signatures consistent with flux ropes to obtain their axis orientation, spacecraft impact parameter, and cross-section size.

The classification criteria are based on the results of the modeling discussed in the previous section. We visually sort the MOs into three broad categories: F, single flux-rope structure; C_x, complex structure with more than one rotation; and, E, ejecta with unclear rotations. For the F-events, we divide them further according to the length of their magnetic field rotations. Thus,

- F_r: Single rotation between 90° – 180°.
- F^-: Single rotation lower than 90°.
- F^+: Single rotation greater than 180°.
- C_x: Multiple rotations.
- E: Unclear rotation.

Figure 5 illustrates the three categories. According to our discussion, an axially symmetric model would be appropriate for the F_r population (*e.g.* October 18, 1995 event in Figure 5a). Deviations from this case are the events with incomplete rotation (F^- population) that could arise from large impact parameter (y_0) crossings (*e.g.* Figure 5b, September 4, 2012 event). Magnetic field rotations larger than 180° (F^+ population) can be interpreted as flux ropes with significant curvature or complex topologies such as a spheromak or a double flux rope (Figure 5c, September 6, 2006 event). The remaining two categories (C_x and E-populations, Figure 5d, 5e) cannot be reproduced by a flux-rope model.

Table 2 reviews the ICME events between 1995 – 2015 listed in Nieves-Chinchilla *et al.* (2018). Each one is tagged according to our classification, *i.e.*, F_r, F^-, F^+, C_x, and E. Figure 6 illustrates the distribution of the categories. At the top, Figure 6a pie charts display
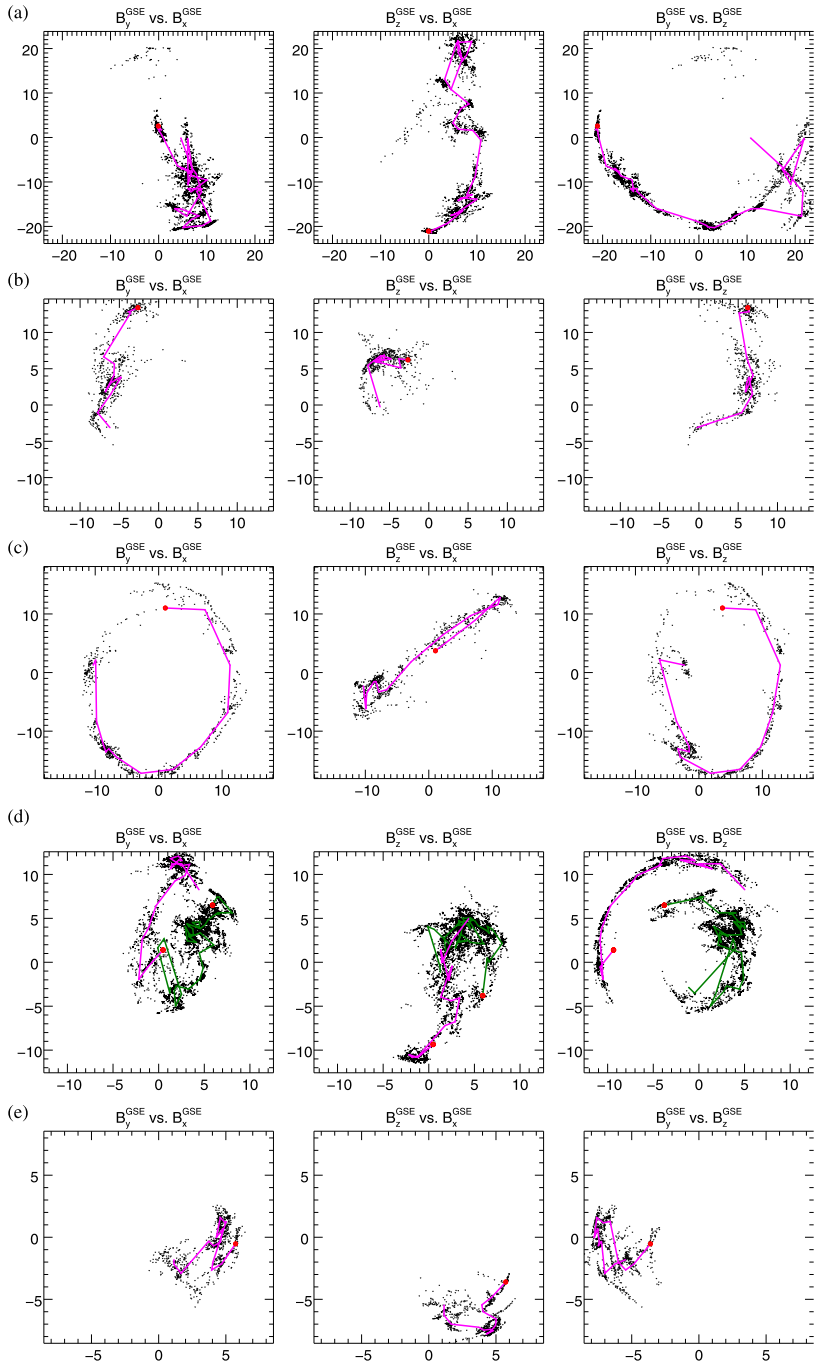
Figure 5 Classification of the magnetic field configurations within the ICMEs observed by *Wind*. From the top: (**a**) a F_r observed on October 18, 1995, (**b**) a F^- observed on September 4, 2012, (**c**) a F^+-event observed on September 6, 2006, (**d**) a C_x observed on February 7, 1995, (**e**) a E observed on February 10, 1997.
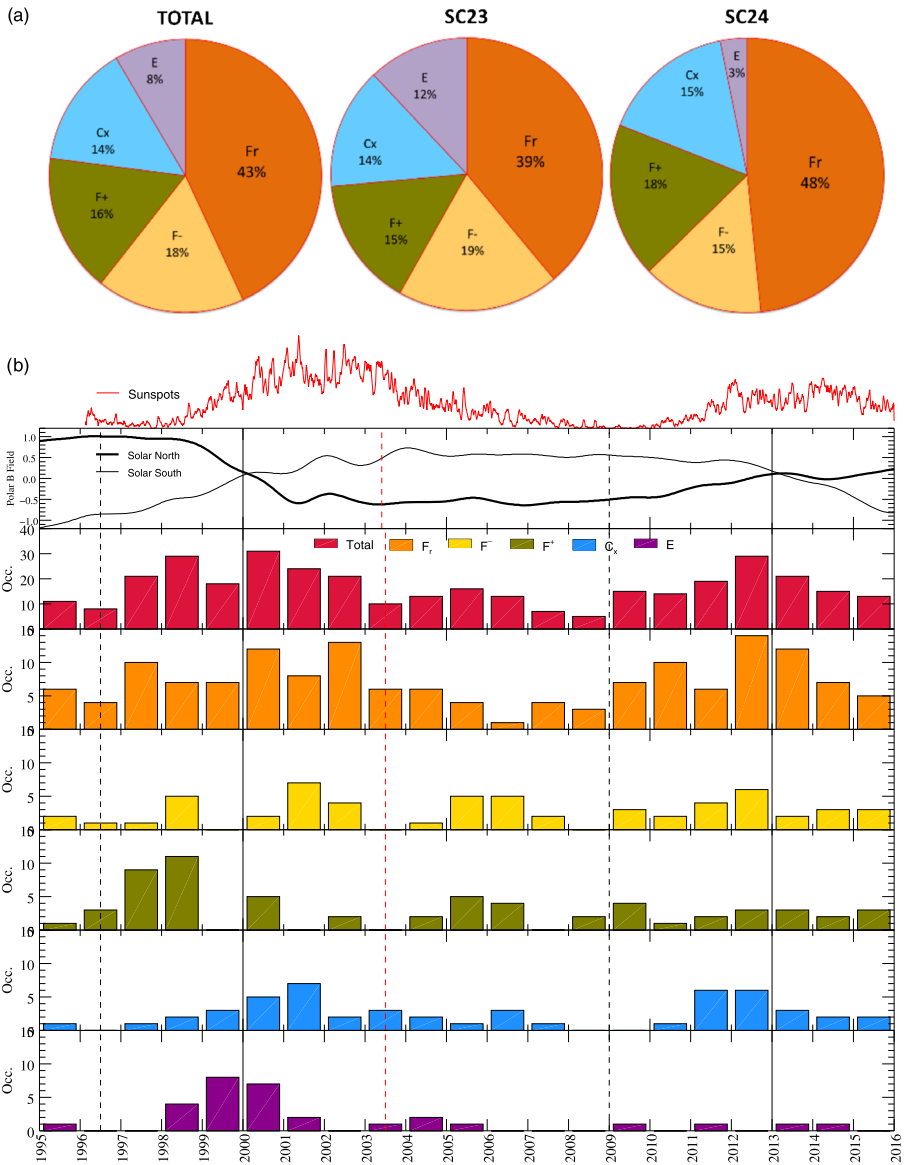
Figure 6 (**a**) Pie chart of ICMEs with signatures of F_r, F^-, F^+, C_x and E for the total period selected (1995–2015), for the Solar Cycle 23 (SC23) and for Solar Cycle 24 (SC24). (**b**) From the top, the sunspot temporal variation (binned to 12 days) for the period selected for the analysis and solar polar field. The *histograms* represent the annual population of the magnetic obstacle (MO) categories and flux-rope species F_r, F^-, F^+, C_x and E. *Dashed vertical lines* indicate the solar cycle minimum, *dotted vertical lines* indicate the solar cycle maximum, and *red dashed vertical line* indicates the same SC23 period to the SC24 period considered in this study.

the total ICME dataset distributions in Solar Cycle 23 (SC23) and 24 (SC24). Figure 6b shows the annual variations of the various ICME types. From top to bottom, we plot the sunspot number variation (binned to 12 days) and the change in the solar polar magnetic field

to evaluate the occurrence of MOs and populations in the solar cycle. The histograms start at the top with the total number of ICME-MO events in red, F_r-events in orange, F^--events in yellow, F^+ in green, C_x in blue, and E in purple. In general, the variation of F_r-events dominates the variation of the total, since they comprise the largest population.

Among the 353 ICME events (Table 2), 77% (272 events) exhibit flux-rope signatures, 14% (51 events) exhibit internal complex structure, and 8% (30 events) are ejectas (see Figure 6a). Similar statistics are evident when considering individual solar cycles with slightly more F-events and C_x-events in SC24 than in SC23 but fewer E-events. For the purpose of comparison, we have added the statistics of SC23 (Table 2, row SC23 short) for the same phase (June 1st, 1996 to May 31st, 2003) on SC24. For the same period we find larger number of events observed during SC23 than SC24. This result is consistent with the sunspot number that indicates stronger solar activity in SC23 than SC24. In a more detailed comparative analysis, the difference is between the number of F-events and E-events, while C_x-events maintain the same ratio. One possible explanation is that E and C_x-events are the consequences of evolutionary processes and are not dependent on the spacecraft trajectory through the MO (see Riley and Richardson, 2013, for instance). This interpretation of higher ratio of F-events is based not only on the number of events but also on the fact that ICMEs during SC24 are weaker (see Gopalswamy *et al.*, 2015; Nieves-Chinchilla *et al.*, 2018; Jian *et al.*, 2018, for instance), in terms of magnetic strength, expansion and bulk velocity, than events in SC23. Therefore, interaction with the ambient solar wind or with other large heliospheric structure, is weaker and has less effect on the ICME's internal structure.

Taking a closer look on flux ropes, 43% carry classic MC signatures with large internal magnetic field rotation (F_r-population). Their percentage is slightly higher in SC24 (48%) *versus* SC23 (39%, 41% in the short period). F^--events constitute 16% of the total ranging from 15% in the SC23 to 18% in the SC24. The percentage of F^+ is the same for SC23 and for total dataset at around 18% and slightly lower in SC24 (14%). Thus, in terms of flux-rope reconstruction under axial-symmetric assumptions, $\approx 43\%$ of the ICME-MO events exhibit the proper signatures, while $\approx 34\%$ display deviations.

The total number of ICME-MOs follows the solar cycle phase in a broad sense. As shown in Figure 6b, there are more events during max than min with a double peaks around the SC23 maximum and during the declining phase. For individual populations, only the sunspot peak in 2001 shows a corresponding F_r peak, the F_r minimum occurs in $2006-2007$, not at the sunspot minimum of 2009, and F_r-events continue to be detected at a rate of $3-4$ events/year even during the deep activity minimum of SC23. During SC24, the F_r is clearly peaked in $2012-2013$ although the sunspot number remains rather flat. However, by comparing the F_r occurrence trend with the solar polar magnetic field, the maximum occurrence in the F_r-populations is consistent with the change in the solar magnetic field polarity. In fact, the minimum in the F_r occurrence is in 2006 that corresponds to the equidistant year between the SC23 and SC24 polarity change. Thus, our results are consistent with the interpretation that flux ropes are mainly responsible for removing the Sun's magnetic helicity and energy. This behavior is consistent with the findings recently discussed by Vourlidas and Webb (2018). They suggest that well-formed flux-rope events (F_r category) must arise from polarity inversion lines outside of active regions and could be, therefore, associated with streamer blowout (SBOs) CMEs. This interpretation should be confirmed by a detailed analysis of pairs of CME-ICME's.

Similar to F^-, the F^+-events represent the main contributors to the double bump in the total number of MOs. The F^+ rates show a strong increase during the rising phase of SC23, when intense flux emergence at lower latitudes and the appearance of magnetically complex active regions may be the reason. However, no such pattern is seen in SC24. Possible expla-

nations are the lower overall eruptive activity (from ARs) and the weaker polar fields that failed to guide CMEs towards the ecliptic as was the case in SC23.

For the remaining cases, although the number of events is low, we can discern some trends. There are more C_x-events around sunspot activity peaks, which seems to be consistent with the larger number of magnetically complex ARs. Those should generate eruptions of equally complex structures that the C_x category represents. On the other hand, only the peak of SC23 shows appreciable number of ejecta. This is consistent with the interpretation of E-events as a result of multi-CME pileups and/or interaction. A large number of CMEs (up to 10 within one day, in some cases) were detected during the SC23 maximum (*e.g.* Vourlidas *et al.*, 2010) but this was not the case in SC24, which is consistent with the much lower E-event rate in SC24.

4. Analysis and Discussion

The basis of the fitting procedure and reconstruction technique has been extensively explained in Nieves-Chinchilla *et al.* (2016). The fitting procedure is based on a Levenberg–Marquardt algorithm to infer the trajectory of the spacecraft in an iterative transformation from the satellite coordinate system to the flux-rope local coordinate system where the model is developed. After setting some initial-guessed parameters, the algorithm has a semi-automatic fitting procedure. Table 5 shows the Earth-directed events observed by *Wind* in the period of 1995 – 2015. The first column lists the events sorted by year followed by the ICME start time (month/day hhmm), decimal day of year, MO start time (month/day hhmm) and MO duration. All the events are also classified as ejecta (E), complex (C_x), or flux rope (F). The flux-rope configurations are identified as F_r, F^- and F^+ following the discussion in the previous section. The mean solar wind speed (V_{sw}) of the MO needed for the reconstruction of the spacecraft trajectory is also included. The table also includes orientation and size for the F-cases; ϕ, longitude; θ, tilt; y_0, impact parameter; and R, cross-section radius. It also contains the goodness of fit parameters: χ^2, chi-square; and the correlation coefficient, ρ.

Figure 7 serves as an example of the fitting procedure. The event was detected on June 27 (178), 2013 at 13:51 UT by the *Wind* spacecraft. The data is displayed in GSE coordinate system, averaged to 15 minutes, and it lasts for 33.62 hours. The event bulk speed is 393 km s^{-1} and exhibits a very slow expansion velocity (7 km s^{-1} as reported by Nieves-Chinchilla *et al.*, 2018). The visual inspection of the event suggests that the configuration is similar to the synthetic data shown in Figure 2d. The magnetic field is dominated by the B_y^{GSE}-component, which implies a highly tilted structure from south to north, which means left-handedness. In the B_z^{GSE}-component there is a slight change in the polarity with $\approx 10\%$ of the MO north oriented right after the spacecraft enters in the flux rope. The B_x^{GSE}-magnetic field component is not completely flat, which indicates a deviation from the perpendicular direction to the Sun–Earth line by an angle ϕ. Because the B_x^{GSE}-component is close to 0, the impact parameters should be close to the flux-rope center.

Table 5 reports the fitting parameters for this example. In agreement with the visual analysis, the orientation of the event is $\phi = 313°$ ($\approx 47°$ away from the Sun–Earth line) and $\theta = -56°$, tilted and pointing southwards. The impact parameter is $y_0 = 0.023$ AU, which is 16% away from the flux-rope center ($R = 0.145$ AU). The chirality is left-handed.

B_x^{GSE} (Figure 7a) depicts the magnetic field strength at the top followed by the three magnetic field components (x, y, z in GSE system). Overplotted with pink line is the output fitting from the reconstruction. A visual inspection of the fitting indicates that the model (pink line) agrees very well with the data, both in the magnetic field strength and the components.

Figure 7 *In situ* magnetic field strength and the GSE components (*black dots*) *versus* time with output model (*pink line*) overplotted. Magnetic field configuration along the tube reconstructed from the model output parameters. The *magnetic field lines* displayed correspond to the distances to the center of $0.20R$, $0.40R$, $0.60R$ and $0.80R$, where R is the flux-rope radius.
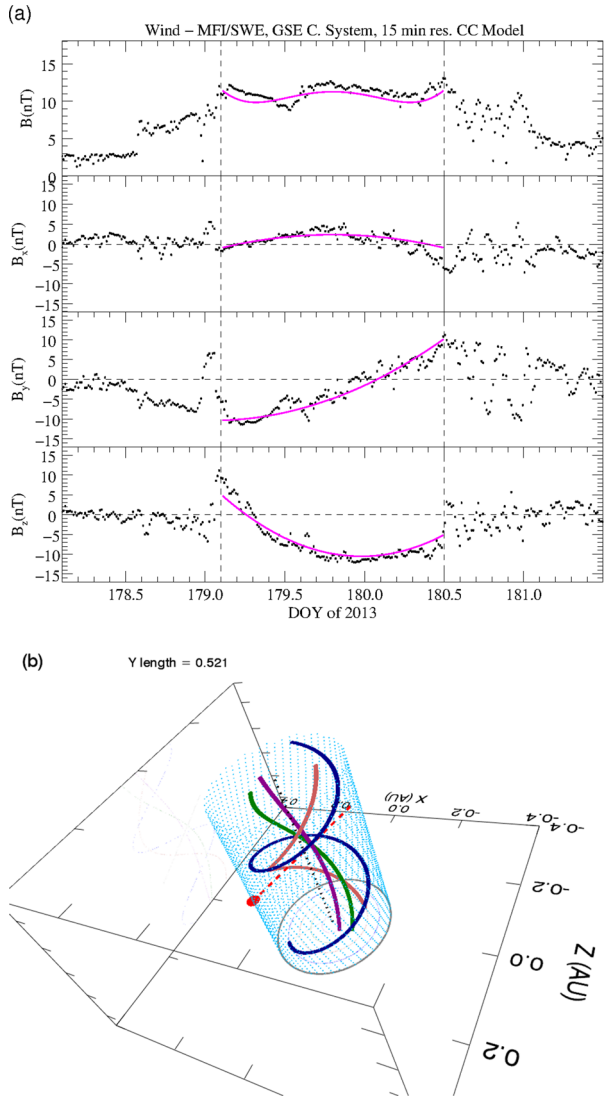
Quantitatively, we report two parameters, ρ, and χ. They are defined as

$$\rho = \frac{\rho_t + \rho_x + \rho_y + \rho_z}{4} \tag{3}$$

where ρ_t, ρ_x, ρ_y, ρ_z are correlation coefficients for each normalized magnetic field dataset (magnitude and x, y, z-components) included in the fitting procedure, and,

$$\chi = \sqrt{\frac{1}{N^2} \frac{\sum_{n=0}^{N} \sum_{i=s,x,y,z} [(B_i^{\text{GSE}} - B_i^{mdl})^2]_n}{(|B|^{\max})^2}} \tag{4}$$

with $i = s$ for the magnetic field strength. In general, as ρ approaches 1 the output fitting become better, and lower χ indicates better fits to the data. In the example event above the
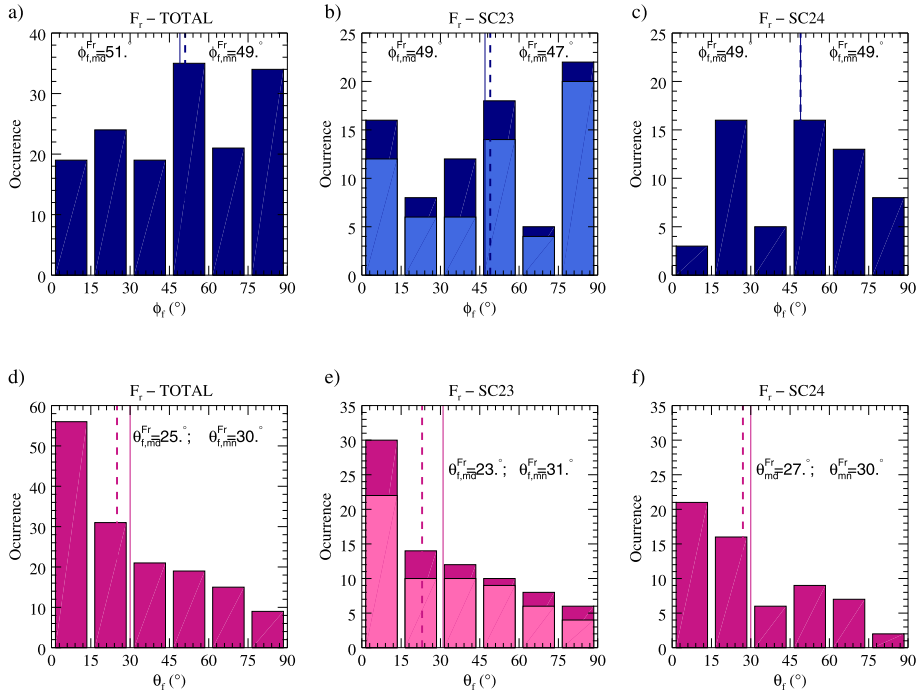
Figure 8 Occurrence of the ϕ_f (*top, blue color*) and θ_f (*bottom, pink color histogram*) angles in bins of 15° for F_r-population. (**a**) and (**d**) display the occurrence for the total number of events, (**b**) and (**e**) during SC23, and (**c**) and (**f**) during SC24. *Vertical line* represents the mean value (mn) and *dashed vertical line* represents the median value (md). The *light color* in (**b**) and (**e**) indicates the comparable phase of SC23 to available phase of SC24.

values are $\rho = 0.893$ and $\chi = 0.209$, which indicate that the fitting is very good/excellent verifying the visual inspection. The *Wind* ICME catalog includes all the events plots, fitting output parameters and reconstruction (see wind.nasa.gov/ICMEindex.php).

4.1. Flux Ropes Orientation

Figures 8 and 9 give an overview of the distribution of the two orientation angles of the F-events. The angles, longitude (ϕ) reported in Table 5 in the range from 0° to 360°, and tilt (θ) in the range from −90° to 90° (Table 5), have been folded to a range from 0° to 90°. For ϕ, the new angle ϕ_f identifies if the flux-rope axis is aligned ($\phi_f = 0°$) or perpendicular ($\phi_f = 90°$) to the Sun–Earth line. For θ, the new angle θ_f identifies if the flux-rope axis is highly tilted (90°) or lies in (0°) the ecliptic plane. Figure 8 shows the F_r-population and Figure 9 the F^- and F^+-populations in 15° bins.

Figure 8a – 8c (dark blue color) shows the distribution of the angle ϕ_f of F_r-population. To compare between solar cycles, we have colored in light blue color the SC23 period corresponding to that of SC24 included in this study. Figure 9a – 9c exhibits the F^-- (blue) and F^+-populations (light blue). In the a-panel the total dataset is shown, in the b-panel the events in the SC23 comparable phase, and in the c-panel the events in SC24 indicated in Nieves-Chinchilla *et al.* (2018). None of the populations exhibit a clear preferred orientation ϕ_f. Note however, in all populations and in the full dataset, the mean ($\phi_{f,\text{mn}} > 45°$) and median ($\phi_{f,\text{md}} > 45°$) values indicate a slight tendency for the axis to be more perpendicular
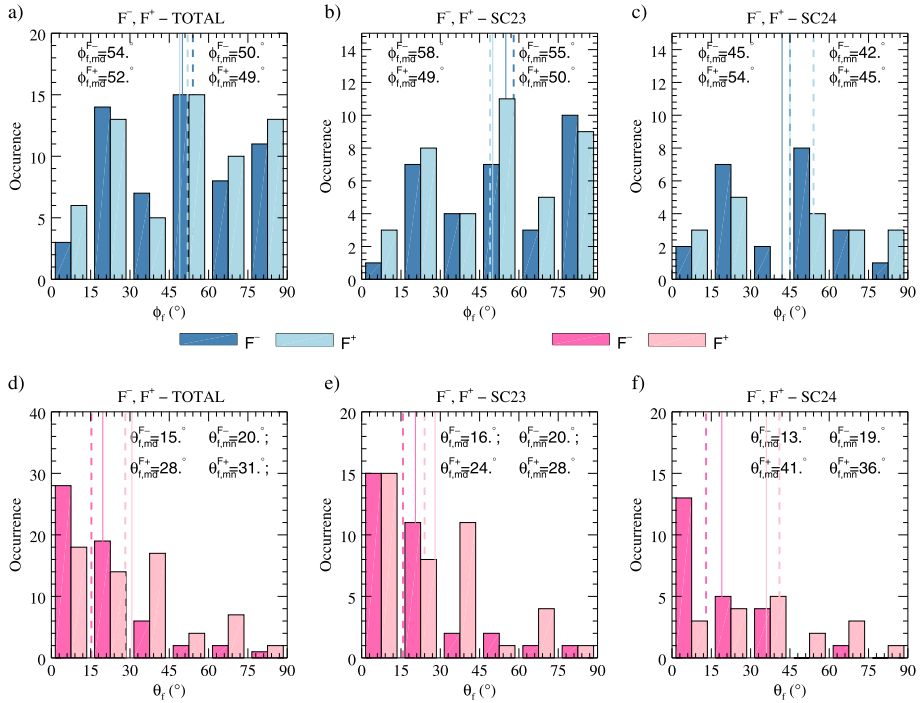
Figure 9 Histograms for ϕ_f (*top, blue colors*) and θ_f (*bottom, pink colors*) values obtained for the two flux-rope species. The colors are grading from darker color for F^-, and light color for F^+. (**a**–**c**) display the total number of events, during SC23, and during SC24 for ϕ_f. (**d**–**f**) display the total number of events, during SC23, and during SC24 for θ_f solid. *Vertical line* represents the mean value (mn) and *dashed vertical line* represents the median value (md) colored according to the population.

to the Sun–Earth line (see Table 4) Table 3 also indicates that in all populations more than 50% of the events are oriented perpendicular to the Sun–Earth line. This could be a selection effect since the magnetic field rotation is better observed as the flux-rope axis becomes more perpendicular.

In Figure 8d – 8f (dark pink color) and in Figure 9d – 9f (pink and light pink colors), distributions of the θ_f angle for the three populations are shown. In Figure 8d – 8f, the histograms represent (d) the total dataset, (e) the SC23 and (f) SC24 dataset events. The in SC23 events falling into the shortened period corresponding to our SC24 event are colored in light pink. The majority of all populations show low tilt ($\theta_f < 30°$). For F_r-population (Figure 8d – 8f), 58% of the events have tilts lower than 30° (Table 3), slightly more occurrence in SC24 with 61% than in SC23 with 56% of the events. The median/mean tilt of the total number of flux ropes studied is $25° – 30°$, showing similar median/mean ($\theta_{f,mn}/\theta_{f,md}$) tilt values in SC23, $23° – 31°$ and in SC24 $27° – 30°$. The comparative analysis between solar cycles, using a similar temporal interval (light pink in SC23), exhibits similar occurrence rate and suggests that the number of events with low tilt increases towards the declining phase in SC24 probably attributed to lower inclination of heliospheric current sheet in the declining phase.

For the other two populations, F^- and F^+, the trend is slightly different. In the case of the F^--population (pink color), the median/mean for the whole dataset is $15° – 20°$, which

Table 3 Statistics of the Direct output parameters.

	P	Total	SC23	SC24
$\phi_f > 45°$	F_r	59%	56%	74%
	F^-	59%	63%	52%
	F^+	61%	63%	56%
$\theta_f < 30°$	F_r	58%	56%	61%
	F^-	81%	81%	78%
	F^+	52%	58%	39%
$\theta_f > 60°$	F_r	17%	18%	15%
	F^-	5%	6%	4%
	F^+	15%	13%	22%

Table 4 Mean (mn) and median (md) values of the flux-rope orientation for the total dataset, Solar Cycle 23 (SC23), and Solar Cycle 24 (SC24).

		θ mn–md	ϕ mn–md
Total	F_r	$25° - 30°$	$51° - 49°$
	F^-	$15° - 20°$	$54° - 50°$
	F^+	$28° - 31°$	$52° - 49°$
SC23	F_r	$23° - 31°$	$49° - 47°$
	F^-	$16° - 20°$	$58° - 55°$
	F^+	$24° - 28°$	$40° - 50°$
SC24	F_r	$27° - 30°$	$49° - 49°$
	F^-	$13° - 19°$	$45° - 42°$
	F^+	$41° - 36°$	$54° - 45°$

is $\approx 10°$ lower than the values for the F_r-population. This difference persists during the two solar cycles. Note that $\approx 80\%$ of the reconstructed events have low tilt (Table 3). In the case of the F^+-population, the median/mean values exhibit similar values to that of the F_r-population and consistently for the whole dataset and for SC23, *i.e.*, $\theta_{f,\mathrm{md}} - \theta_{f,\mathrm{mn}} = 28° - 31°$ and $\theta_{f,\mathrm{md}} - \theta_{f,\mathrm{mn}} = 24° - 28°$, but slightly higher for SC24 with $\theta_{f,\mathrm{md}} - \theta_{f,\mathrm{mn}} = 41° - 36°$.

Figure 10 exhibits the annual normalized occurrence of events with $\phi_f > 45°$ and $< 45°$ in the top two panels with blue colors and $\theta_f > 30°$ and $\theta_f < 30°$ in the two bottom panels with pink colors. The three set of panels (a–c) represent the three populations: (a) with dark blue/pink for the F_r-population, (b) with blue/pink for the F^--population, and (c) with light blue/pink color for the F^+-population. For each population the temporal variation of the sunspots is included in two panels (red or blue color line) to help evaluate the trend relative to the solar cycle variation. Between the top two and bottom two panels, we have also included the heliospheric current sheet (HCS) tilt in order to evaluate the effect of the large scale magnetic field in the flux-rope orientation.

Based on visual inspection of the figure, the F_r-population shows solar cycle trend *vs.* the other two populations in both angle orientations, ϕ_f and θ_f. In the case of ϕ_f, (top panel of Figure 10a) the occurrence rate of flux ropes with a perpendicular axis to the Sun–Earth line increases during the rising phase of solar cycles. An occurrence decrease in the second panel can be identified for the same period. The effect is most significant during the SC22 minimum and SC23 rising phase. Near solar maximum and in the early declining phase in
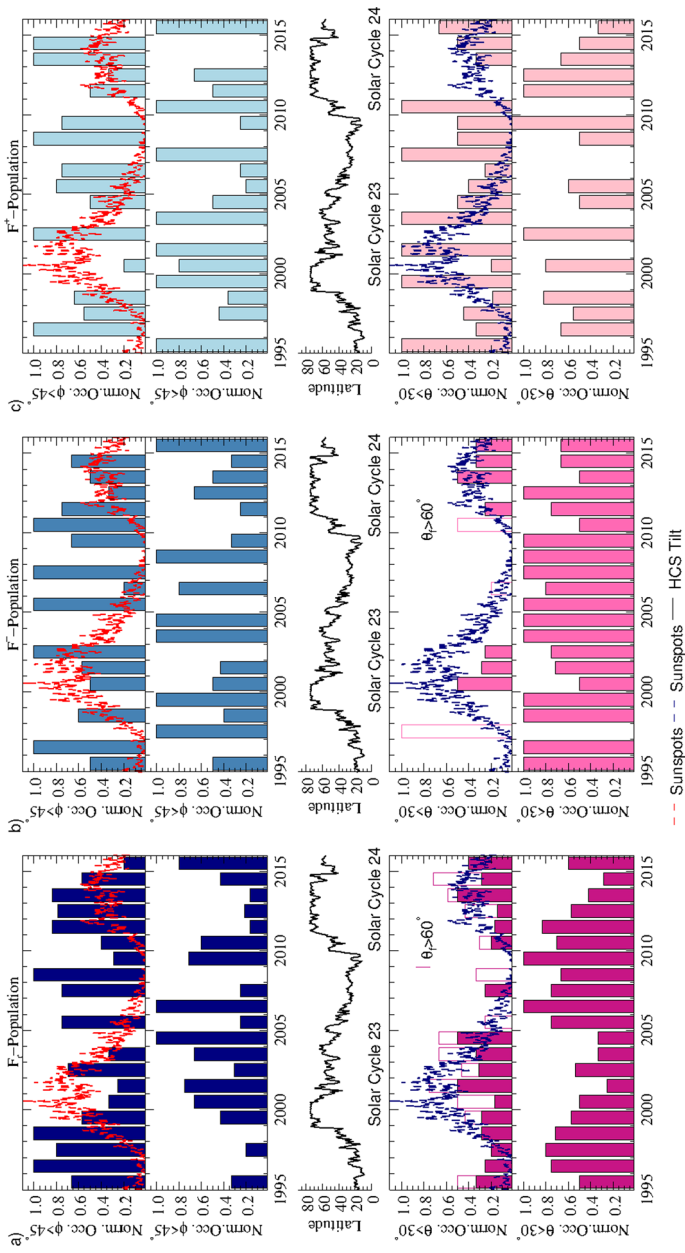
Figure 10 Annual normalized angular occurrence for the three populations: **(a)** F_r-population, **(b)** F^--population, and **(c)** F^+-population. From the top, the occurrence of events with $\phi_f > 45°$ at the top, occurrence of events with $\phi_f < 45°$, latitude of heliospheric current sheet, occurrence of events with $\theta_f > 30°$; and, at the bottom, occurrence of events with $\theta_f < 30°$.

SC23 (2000–2005), the top panel exhibits lower occurrence rate probably because solar wind disturbances.

Previous studies have explored the solar cycle dependency of the magnetic field polarity within MCs (Mulligan, Russell, and Luhmann, 1998; Li *et al.*, 2011, 2014; Li, Luhmann, and Lynch, 2018). In these studies the identification of the high or low inclined flux ropes was based on visual inspection and they did not attempt to measure the MC flux-rope inclination angle. We have plotted the θ_f angle (pink color) in the two bottom panels of Figure 10. Our analysis shows that there is a clear flux-rope inclination dependence with respect to the solar cycle in the F_r-population (Figure 10a, two bottom panels, pink bar plots) and no clear dependence in the other two populations (Figure 10b, 10c). Pink bars show the annual occurrence of the events with tilt $> 30°$. Each bar is divided into cases with $30° < \theta_f < 60°$ with pink color and crowning each bar is the occurrence of events with higher inclination, *i.e.*, $\theta > 60°$ (white bar). The $\theta_f > 60°$ cases are the most probable and exhibit north or south polarity under a certain combination with ϕ while the $30° < \theta_f < 60°$ cases display bipolarity. Over plotted, with blue line, is the SSN to follow the solar cycle trend and in between the longitude and tilt is plotted the HCS tilt angle obtained by WSO of Stanford based on a potential-field source-surface (PFSS) model. The highly tilted events reach a frequency of $\approx 80\%$ during 2003 and 2014, in the early declining phase of SC23 and SC24.

In the bottom panel the annual occurrence of low-tilted events ($\theta_f < 30°$) colored with pink color is shown. These are the cases where the B_z^{GSE}-component will display a double sign or bipolarity, *i.e.*, NS or SN, unless the axis is aligned with the Sun–Earth line. They show solar cycle dependency with minimum occurrence around the maximum in both solar cycles for the F_r-population. It is important to note that, in contrast to the high inclined events, the occurrence of low-tilted events are more frequent with a systematic $\approx 20\%$ of the cases observed during the maximum solar cycles periods studied.

Finally, we want to explore if there is any remote sensing signature of the CME inclination. Figure 11a shows the not stacked barplot with the normalized occurrence of CMEs with angular width (AW) larger than $60°$. The set includes 1185 events from the dual-viewpoint CME catalog based on COR2 data (Vourlidas *et al.*, 2017). All events are treated equally, *i.e.*, no distinction regarding their apparent morphology in the coronagraph images is made. The angular widths are projected measurements based on single viewpoint images. The proportion of CMEs exhibiting AW larger than $60°$ clearly varies with the solar cycle. Wide CMEs (AW $> 60°$) dominate at times of solar maxima, increasing the occurrence as the global configuration of the Sun's magnetic field becomes more complex. Balmaceda *et al.* (2018) reports that CMEs with clear signatures of flux ropes (presence of a cavity, three-part structure, *etc.*) exhibit typical widths of $\approx 50°$, in agreement with previous results on the average CME width (Yashiro *et al.*, 2004; Vourlidas *et al.*, 2010). Loop CMEs, on the other hand show an average width almost $2\times$ larger ($\approx 90°$) and are interpreted as flux-rope CMEs seen face-on. Thus, an interpretation is that around the maximum more CMEs exhibit larger inclinations and therefore they are seen projected on the plane of sky as wide structures. By comparing this result with our analysis for the same period of time (Figure 11b) they broadly correlate with systematic increases of wide CME and high inclined flux ropes around the maximum. However, the number of CMEs with AW $> 60°$ increases during the years 2010–2012 and slightly decreases afterwards. In the case of the flux ropes, the highly inclined increases more after 2012. We interpret this comparative result as an effect of an evolutionary process; the highly inclined CMEs are accommodated to the HCS tilt suffering deflections or rotations in the journey at 1 AU. In any case, this finding leads us to questions such as how, when and why some flux ropes are affected by the surrounding magnetic field configurations, and if it is related to the source region, by initial stages or by propagation processes.

Figure 11 Comparative analysis of the normalized occurrence during 2007 – 2014 of CMEs with angular width (AW) greater than 60° and the high tilted flux ropes with $\theta > 30°$. The CMEs AW measurements are taken from the CME catalog based on COR2.
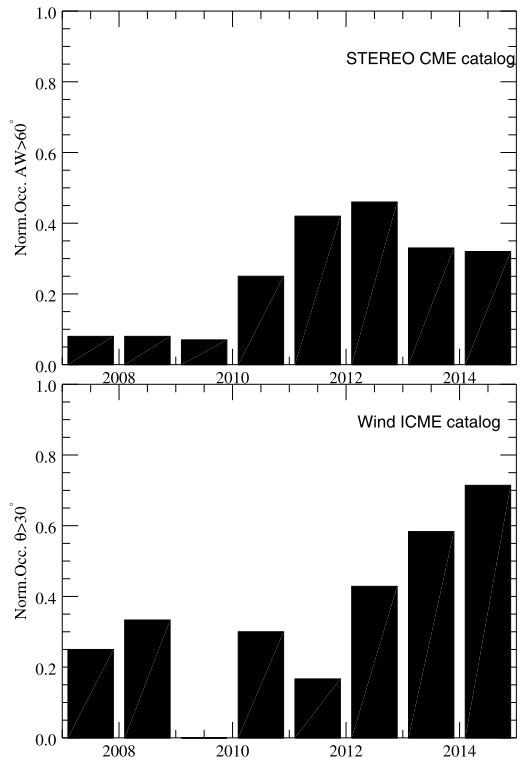
4.2. Magnetic Bipolar or Unipolar Configuration

Figure 12 displays the annual normalized occurrence of bipolar or unipolar magnetic configuration of the F-events and the solar polar magnetic field. The SN or NS classification has been done according to the discussion and definition given in Figure 4 and Table 1. The figure is crowned by the solar polar magnetic field and SSN to follow the change in the solar magnetic field polarity and solar cycle trend. Among the 272 F-events, 103 events (38%) are NS, 106 events (38%) are SN, 24 events (9%) are N and 39 events (14%) are S. The identified NS and SN bipolar events include the mostly S or N events since the dataset is not large enough to evaluate the different configurations. Thus, during the 21 years of data, almost two solar cycles, we have found almost an even number of opposite bipolar configurations and opposite unipolar configurations.

A visual inspection of Figure 12b reveals a smooth change in the polarity in the bipolar flux-rope configurations. The flux-rope polarity changes from SN in the rising phase of the SC23 towards NS in the declining phase to dominate during the SC24 rising phase. Around the solar cycle minima the configurations, either SN (SC23) or NS (SC24), almost exclusively dominate. The number of events with N or S configuration increases around the solar cycle maximum and declining phase consistently with the number of events with tilt $> 30°$ (Figure 10). These results confirm the findings of Li *et al.* (2011, 2014), Li, Luhmann, and Lynch (2018) based on visual identification of the flux-rope polarity. There is a cyclic reversal of the bipolar MC poloidal field on the same time scale of the solar magnetic cycle. These results suggest that CMEs could remove the latest solar cycle magnetic field and helicity (Low, 2001; Gopalswamy *et al.*, 2003).

Figure 12 From the top.
(**a**) Annual distribution of the
sunspot number in red and polar
magnetic field. (**b**) Annual
normalized occurrence of the NS
(positive) and SN (negative)
configurations. (**c**) Annual
normalized occurrence of the N
(positive) and S (negative)
configurations. (**d**) Annual
normalized occurrence of the
right-handed (positive) and
left-handed (negative)
configurations.
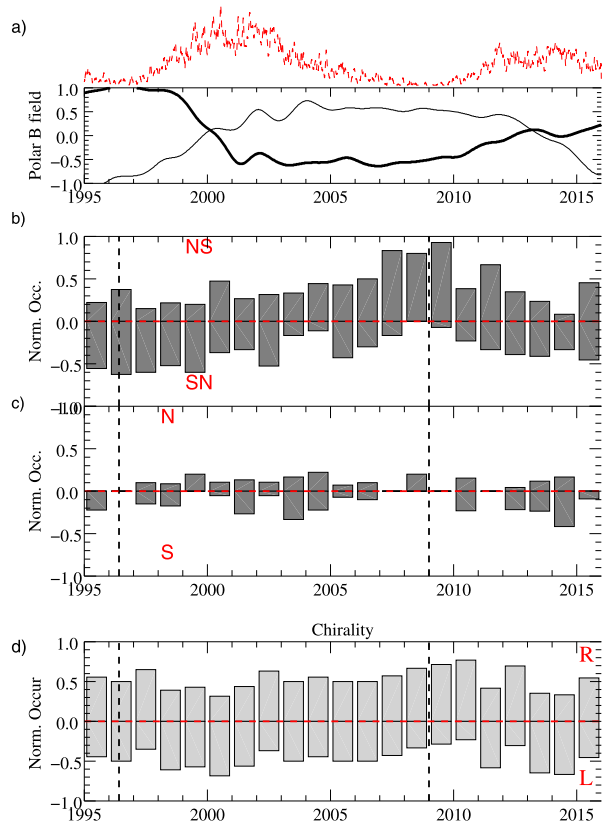
In Figure 12d, the annual normalized occurrence of the chirality is shown. The positive values indicate the right-handed events and negative values left-handed and visual inspection of the plot does not reveal a clear solar cycle trend. This result suggests that the bipolarity is only due to the orientation of the flux rope.

4.3. Spacecraft Impact Parameter and Cross-Section Size

Figure 13 displays the normalized occurrence of impact parameter (y_0/R) (a) for F_r-population (first column), (b) F^--population (second column) and (c) F^+-population (third column). The bin size of the histogram is 0.2 of the radius from the flux-rope center. Thus, at 0 the spacecraft crosses through the flux-rope center, while at 1 the spacecraft crosses through the flux rope edge. In the case of the F_r-population, Figure 13a, the occurrence of the impact parameter is distributed along all possibilities with a slight increases ($\approx 25\%$) around the flux rope center ($0 - 0.2$) and flux rope edge ($0.8 - 1.0$). In the case of F^--population, Figure 13b, the results are consistent with the initial hypothesis that the F^--events are flux ropes crossed by the spacecraft with high impact parameter. However, in the case of the F^+ population, the model interprets that the spacecraft is crossing closer to the flux-rope axis. These results does not shed any light to the debate between Lepping and Wu (2010) and Démoulin, Dasso, and Janvier (2013). The first authors found a progressive decrease of the identified MCs as the impact parameter increases. The second group demonstrated mathematically that there is not a fundamental basis for such result.
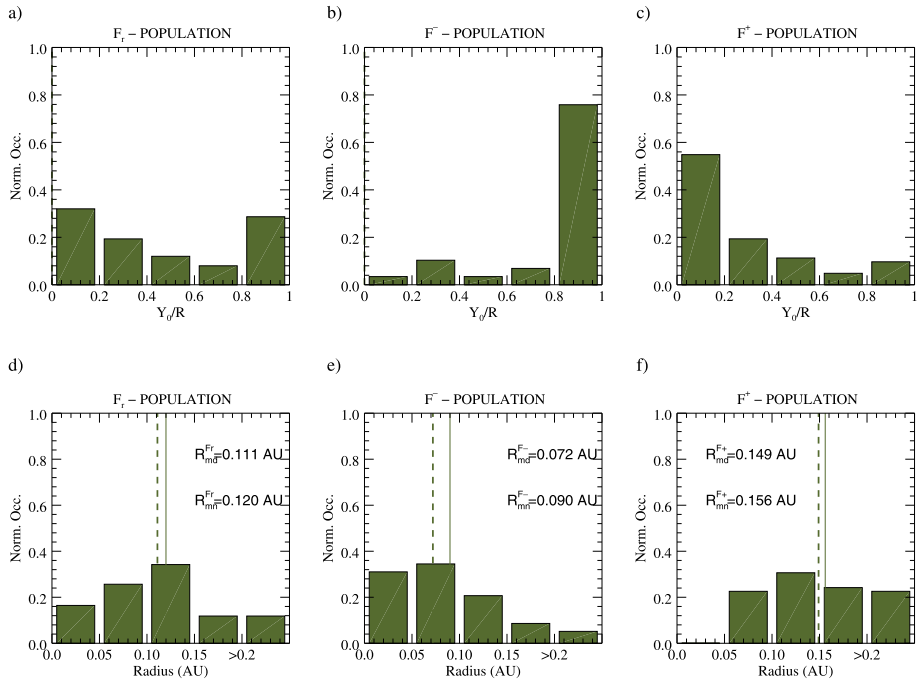
Figure 13 Percentage of the impact parameter (y_0/R) occurrence for (**a**) F_r-population, (**b**) F^--population, and (**c**) F^+-population. The impact parameter (Y_0) has been scaled to the flux-rope size (R). Percentage of the size (R) occurrence for (**d**) F_r-population, (**e**) F^--population, and (**f**) F^+-population.

Finally, the bottom panel in Figure 13b shows the normalized occurrence of flux-rope radius (R). This is a derived quantity from the reconstruction. In all cases, the range of values vary between $0 - 0.2$ AU on average, however, the mean/median values of each population show different values. While the F_r-events show a mean/median value of 0.11 AU, the F^- population is smaller with values of $\approx 0.07/0.09$ AU and the F^+ population is larger with a value of ≈ 0.15 AU.

5. Summary, Conclusions and Final Remarks

The understanding of the magnetic field configuration in CMEs is primarily based on the assumption that their internal structure are flux ropes. In this paper, we conduct a study to better understand the internal magnetic field structure of ICMEs and analyze the intrinsic properties of the magnetic obstacles at 1 AU. We undertook a comprehensive study of events observed by *Wind* in the period of $1995 - 2015$. These events are characterized by periods of increased magnetic field strength, smooth internal change in the magnetic field direction and the existence of plasma cooler than the surrounding solar wind. We defined these structures as low-β magnetic obstacles (MOs).

As reported by Nieves-Chinchilla *et al.* (2018), the expected configuration of the internal ICME magnetic flux-rope structures do not always exhibit the rotation in magnetic field direction. Such structures with unclear flux-rope signatures are variously defined in the literature as "magnetic-cloud-like", "flux-rope-like" or "non-classic-magnetic-cloud". The MO term is introduced to reduce confusion as a unifying replacement for all these terms.

In the first part of this paper, we simulate the magnetic configurations for various flys through a circular–cylindrical flux-rope structure. We create and analyze synthetic data based on the circular–cylindrical flux-rope model and 3D reconstruction of Nieves-Chinchilla *et al.* (2016). The free parameters in the simulation are the longitude (ϕ), tilt (θ), impact parameter (y_0) and chirality ($H = +$ or $H = -$) of the flux rope. We compile and discuss various magnetic field configurations (unipolar, bipolar or hybrid) and the *in situ* signatures observed for different spacecraft crossings. We discuss the effect of large impact parameters on the chirality or handedness.

With an eye to space weather needs, we study in detail (Section 2.2) the flux-rope orientations resulting in bipolarity in the B_z component. We define intervals for a pure bipolar configuration when B_z is 30% to 70% positive/negative during the first half of the spacecraft transit through the flux rope and 70% to 30% negative/positive in the second half. In this configuration the B_y component is mostly positive (negative) when the flux rope is eastwards (westwards), respectively. We define mostly-north or mostly-south bipolar configuration when the B_z component changes polarity but remains for most of the time (70% – 90% of the crossing duration) positive (mostly-north) or negative (mostly-south). Most of these cases are within the previously hybrid configurations where both the B_z and B_y display bipolarity. One important conclusion from this analysis is the longitude of the flux-rope axis plays a significant role and should be taken into account to predict the critical B_z bipolarity.

In the second half of the paper, we conduct a detailed classification of the observed patterns in MOs by comparing the 353 ICMEs observed by *Wind* to the synthetic observations, we sort the ICME samples in three broad categories based on the magnetic field rotation pattern. Namely, as shown in Figure 5, we identify events without obvious rotation (E), events with single magnetic field rotation (F), and events with more than one magnetic field rotation (C_x). In other words, the F types are events closely following the expectations from a magnetic flux rope.

We further subdivide the F-population in three groups based on the angular span of the magnetic field rotation: i) F_r-events exhibit rotation between $90 - 180°$; cases most amenable to reconstruction with axially symmetric flux-rope geometries; ii) F^- types exhibit shorter rotations and are primarily cases with large impact parameters; iii) F^+ types that exhibit rotations $> 180°$ and obviously deviate from an axially symmetric geometry. The F^+-events may represent events with significant curvature or distortion (Nieves-Chinchilla *et al.*, 2018). It would be interesting to explore whether other magnetic structures such as spheromak or double flux ropes give rise to such structures.

In the analysis of the internal magnetic field configuration we find that:

- From the 353 ICMEs with MOs, 272 are F type ($\approx 77\%$ of the total) and can be associated with flux-rope structure. The remaining 23% exhibit internal complexity (C_x and E). There are more complex events around sunspot activity peaks, which seems consistent with the larger number of magnetically complex ARs. Complex events are more prevalent during the peak of SC23. This suggests that complexity arises as the result of multi-CME pileups and/or interaction. A large number of CMEs (up to 10 in a single day) were detected during the SC23 maximum (*e.g.* Vourlidas *et al.*, 2010) but this was not the case in SC24, which is consistent with the much lower complexity rate in SC24. Thus, evolutionary processes, such as interaction or erosion, can be the main cause of difference between coherent flux-rope structures and complex, but also, it should be important for future studies to take into account the solar source and initiation processes of such CMEs.
- Within the non-flux-rope events, we find 51 C_x cases (14%) and 30 E cases (9%) that display different intrinsic complex signatures. This statistics is basically consistent in the solar cycles. In the first group, the internal magnetic configuration displays magnetic

substructures that could be reproduced by a more complex model than a single-flux-rope model. The second group does not show any coherent or systematic signatures.

- Of the F types, the F_r cases (152 events, $\approx 43\%$) display the expected signatures of a flux rope with axial-symmetric geometry. The other two types can also be considered flux ropes under some assumptions. The F^- cases (16%) are considered flux ropes crossed by the spacecraft with very large impact parameter and therefore there is not a full magnetic field rotation. This assumption is also interpreted by the model in the fit with 78% of the cases with large impact parameter. The F^+ cases (18%) can be considered single flux ropes by assuming that the curvature is significant. These cases can be considered also spheromak structure but this feature needs to be further explored in future studies. Using reconstruction with the circular–cylindrical geometry, the model interprets these cases with small impact parameter, *i.e.*, the spacecraft crosses close to the flux-rope center. In terms of the size, the model interprets that the F^- are the smallest structures (median of the dataset ≈ 0.072 AU) and the F^+ are the largest (median of the dataset ≈ 0.149 AU). The F_r median size is 0.111 AU.

- ICME rises and falls with the solar cycle following, in a broad sense, we have a solar cycle trend with a double small bump at the end of the declining phase of the SC23. In the case of the F_r the minimum of occurrence corresponds to the period of stability in the middle declining phase. In the interpretation of the small increase in the number of F^-- and F^+-events around this period we could speculate that the origin and intrinsic structure of such events are different of the F_r but to confirm this hypothesis a systematic analysis of the solar source is required.

- The F^+ rate strongly increases during the rising phase of SC23. Intense flux emergence at lower latitudes and the appearance of magnetically complex active regions may be the reason for this. No such pattern is seen in SC24. Possible reasons are the lower overall eruptive activity (from ARs) and the weaker polar fields that failed to guide CMEs towards the ecliptic as was the case in SC23.

In the analysis of the orientation of the ICMEs based on the reconstruction described by Nieves-Chinchilla *et al.* (2016), the main findings and conclusions can be summarized as follows:

- More than half of the F_r-events display low tilt ($\theta < 30°$) for the whole dataset and by solar cycles. This number increases significantly in the case of the F^- type events. This inclination is more likely to display the range of bipolar B_z configuration for almost all longitudes (more aligned with Sun–Earth line, less B_z rotation). On the other hand, only $\approx 17\%$ of the F_r-events show high inclination ($\theta > 60°$), with ensured B_z unipolar configuration. Thus, according to our results, most of the cases are deflected at 1 AU but the F^- are more susceptible than any other type of flux ropes.

- We find that both longitude and tilt follow the general trend of the solar cycle for the F_r type of events. The other two populations do not show a solar cycle trend.

- In the case of the tilt (θ), the F_r follow the SSN trend and the HCS tilt, with maximum tilt ($> 60°$) around the maximum in the SSN and remain high occurrence of highly tilt flux ropes ($> 30°$) during the declining solar cycle phase consistently with HCS tilt. Therefore, there is more chance to find B_z magnetic bipolar configuration around the minimum.

- By comparing the occurrence of highly tilt flux ropes ($\theta > 30°$) with the occurrence of CME with wide angular (AW) width ($\theta > 60°$) observed remotely with STEREO during $2007 - 2014$, we have found that they broadly correlate. The number of events with AW $> 60°$ increases during the $2010 - 2012$, years of high solar activity, and slightly decreases afterwards. In our analysis, the highly inclined flux ropes ($\theta > 30°$) increases in

2012. These results suggests two things: the solar cycle variation of the angular width could provide information about the flux-rope orientation in the early stages of the CME evolution, and, the shift between the maximum occurrence of CME with large angular width and highly tilted flux ropes could be an effect of the evolutionary processes, *i.e.*, the highly inclined CMEs are accommodated to the HCS tilt suffering deflection or rotation in the evolution throughout the heliosphere.

- The analysis of flux-rope configurations show that the events with B_z magnetic bipolar configuration clearly follow the solar cycle trend suggesting that the CMEs could be responsible for removing the magnetic field and helicity from the Sun. This result confirms previous studies based on visual inspection.
- The annual occurrence of the left- or right-handed chirality does not show a clear trend with the solar cycle. This result confirm that the solar cycle trend in the B_z magnetic bipolarity is solely due to the orientation of the flux rope.
- In the case of unipolar configuration, the number of N/S configurations increases around the solar cycle maximum and declining phases consistently with the number of events with tilt $> 30°$ but shows no other strong cycle trends or privileged orientation N or S in the solar cycles.

This work is an attempt to reconcile the observations of the heliospheric flux ropes and the modeling by exploring the limitations in the models and in the observations. We are constrained to exploring the internal magnetic field structure of the CMEs by figuring out the magnetic configurations. The strong limitation of 1D *in situ* observations from instruments onboard satellites prevents us from complete view of the structure. Thus, we have to infer flux-rope structures based on single monotonic changes in the magnetic field in spite of that they do not always display the expected magnetic field configuration associated with flux-rope internal structure. In this paper we cannot confirm if all CMEs are flux ropes, or whether more complex structures, or evolutionary processes have affected the internal structure, it is necessary to expand the analysis with larger dataset, to combine this kind of studies with systematic multi-view, and multipoint analyses. The Parker Solar Probe mission (Fox *et al.*, 2016) and the future Solar Orbiter mission (Müller *et al.*, 2013) will aid to shed some light on this dilemma with conjunctions with other missions and by exploring the first stages in the evolutionary processes. Finally, another aspect to take into account in the fact that the current analytical models and *in situ* reconstruction techniques are limited to reproduced structures with well-organized internal magnetic field and well-defined geometry. However, a realistic and more intuitive view of the heliospheric flux ropes can be described in terms of a confined magnetized plasma within magnetic field lines wrapping around an axis in a twisting but not necessarily a monotonic way. It is important to review the current status of the models and adapt them to our current understanding of the heliospheric flux-rope topology and geometry.

Appendix: *In situ* Imprints of the Magnetic Field Flux-Rope Configurations
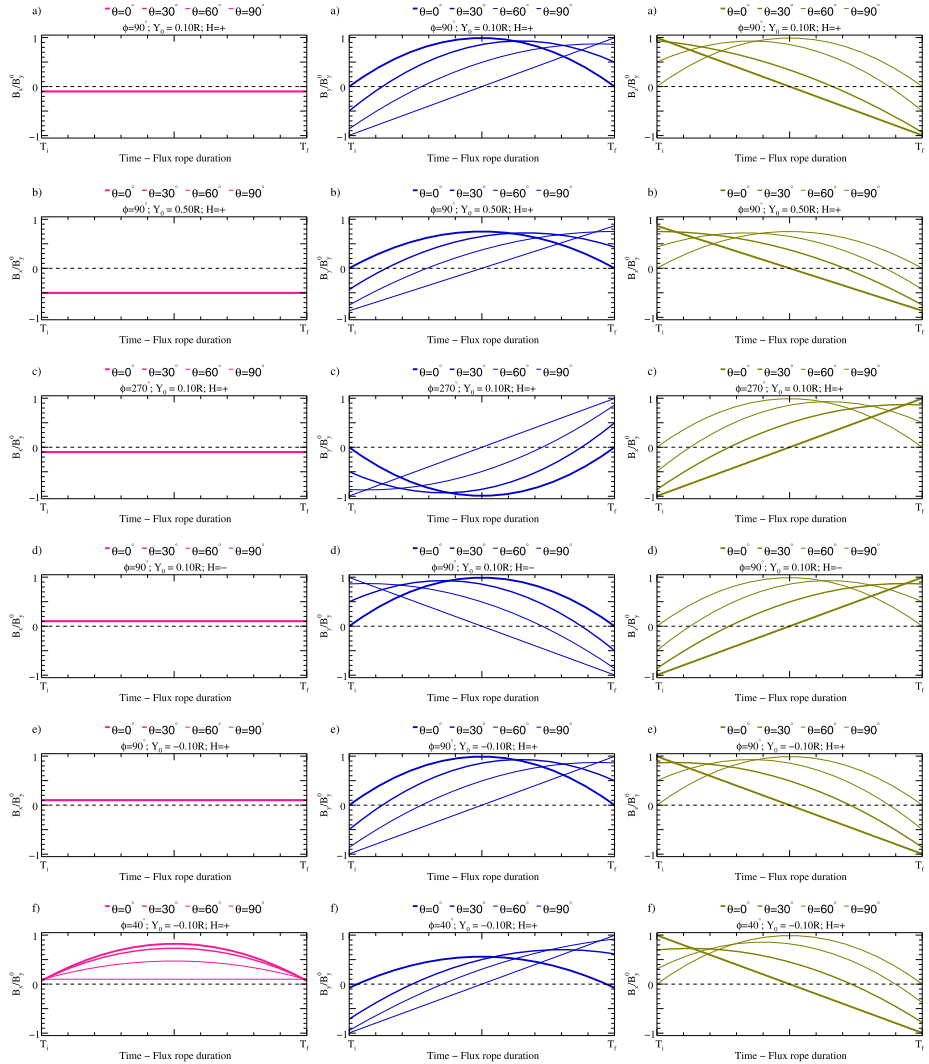
Figure 14 Internal magnetic field configurations.
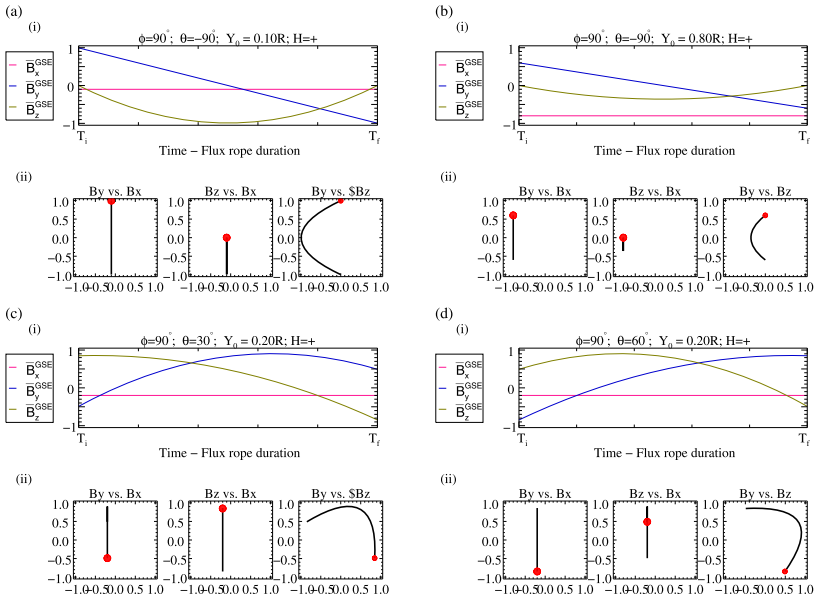
Figure 15 (**a**) *In situ* signatures in the GSE coordinate system and sketch representing the west-north-east, right-handed (WNE-RH), (**b**) representing the east-north-west, left-handed (ENW-LH), (**c**) east-south-west, right-handed (ESW-RH), and (**d**) west-south-east, left-handed (WSE-LH). For each configuration is included: (**i**) Temporal variation, (**ii**) magnetic hodograms of the GSE magnetic components.
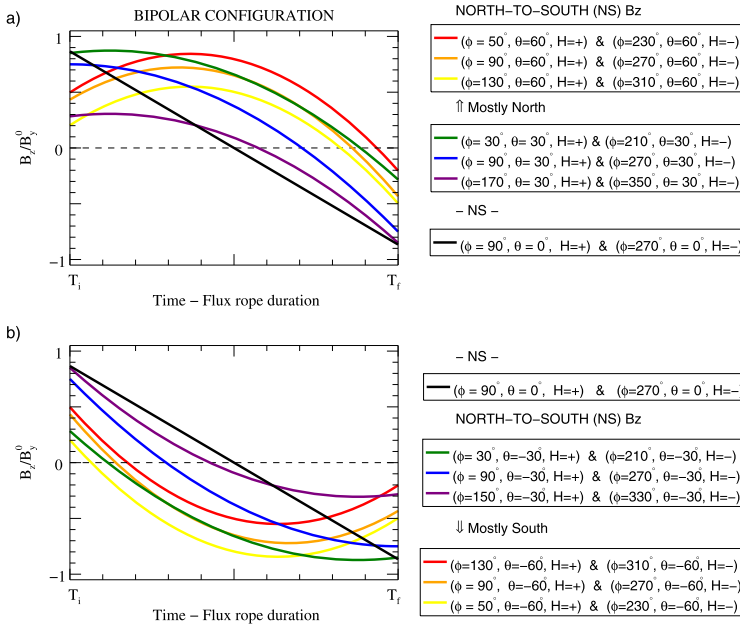
Figure 16 Combination of flux-rope axis configurations; longitude (ϕ), tilt (θ), and chirality (H) fixing the impact parameter (Y_0) $= 0.50R$ to obtain a bipolar B_z configuration normalized to the central magnetic field, B_y^0.

Table 5 Catalog of ICMEs observed by Wind from 1995 to 2015. Column: (1) event number; (2) year; (3) ICME – disturbance arrival time, DOY and magnetic obstacle arrival time; (4) duration; (5) MO type; (6) MO bulk velocity (km s^{-1}); (6) magnetic field configuration; (7) longitude (ϕ); (8) tilt (θ); (9) impact parameter (Y_0); (10) radius (R); (11) goodness of the fitting (χ^2); and (12) correlation coefficient (ρ).

E	Year	ICME$_s$ (DOY) MO$_s$	ΔT_{MO} hrs	MO	V_{sw} km s^{-1}	H	Conf.	ϕ (°)	θ (°)	y_0 (AU)	R (AU)	χ^2	ρ
1	1995	02/07 1911 (38) 02/08 0321	66.25	C_x									
2		03/04 0036 (63) 03/04 1123	15.73	F_r	443.7	L	S	212.	−79.	−0.055	0.096	0.258	0.617
3		03/06 0211 (65) 03/06 0711	19.20	F^-	458.8	R	NSN	155.	15.	−0.223	0.228	0.157	0.498
4		04/03 0643 (93) 04/03 1245	24.68	F^+	294.1	R	NSS	116.	−34.	0.098	0.123	0.385	0.485
5		04/05 0711 (95) 04/05 1759	23.28	F_r	332.1	L	SN	97.	1.	0.065	0.109	0.285	0.767
6		05/13 1019 (133) 05/13 1019	5.68	E									
7		06/30 0921 (181) 06/30 1423	50.40	F_r	398.0	R	SN	306.	5.	0.176	0.262	0.444	0.563
8		08/22 1256 (234) 08/22 2219	20.40	F_r	359.4	R	SNS	263.	−31.	0.034	0.092	0.308	0.638
9		09/26 1557 (269) 09/27 0336	17.75	F_r	375.6	L	S	13.	−33.	−0.101	0.109	0.447	0.157
10		10/18 1040 (291) 10/18 1911	31.20	F_r	407.4	R	SN	294.	−8.	−0.007	0.135	0.197	0.626
11		12/15 1452 (349) 12/16 0711	12.00	F^-	396.5	L	SNN	69.	15.	0.032	0.058	0.405	0.460
12	1996	02/15 1507 (46) 02/15 1507	17.87	F^+	387.0	L	SNS	102.	−55.	0.010	0.079	0.496	0.446
13		04/04 1159 (95) 04/04 1159	9.62	F_r	388.6	R	SNN	279.	25.	−0.024	0.048	0.346	0.649
14		05/16 2247 (137) 05/17 0136	10.38	F^+	419.9	L	NS	251.	−16.	0.031	0.057	0.424	0.466
15		05/27 1445 (148) 05/27 1445	35.63	F_r	368.0	L	SN	51.	−3.	−0.118	0.166	0.223	0.318
16		07/01 1305 (183) 07/01 1716	17.02	F_r	354.0	L	SN	89.	3.	−0.023	0.072	0.304	0.689
17		07/02 1604 (184) 07/02 1604	6.72	F^-	395.1	R	NSN	147.	24.	0.008	0.021	0.430	0.702
18		08/07 0823 (220) 08/07 1159	25.22	F_r	345.2	R	SNS	260.	−40.	−0.066	0.119	0.353	0.601
19		12/24 0126 (359) 12/24 0307	32.63	F^+	348.3	R	NSN	105.	23.	0.039	0.136	0.205	0.805

Table 5 *(Continued)*

E	Year	ICME$_s$ (DOY) MO$_s$	ΔT_{MO} hrs	MO	V_{sw} km s^{-1}	H	Conf.	ϕ (°)	θ (°)	y_0 (AU)	R (AU)	χ^2	ρ
20	1997	01/10 0052 (10) 01/10 0447	22.33	F^+	436.8	R	SN	246.	−11.	0.012	0.102	0.156	0.857
21		02/09 1250 (40) 02/10 0252	15.60	F^-	456.8	R	S	196.	−66.	−0.364	0.371	0.327	0.277
22		04/10 1702 (100) 04/11 0545	13.43	F_r	462.9	R	NSN	177.	14.	−0.043	0.046	0.327	0.245
23		04/21 1011 (111) 04/21 1159	43.20	F^+	362.1	R	SN	322.	12.	0.012	0.118	0.393	0.808
24		05/15 0115 (135) 05/15 1000	16.63	F^+	470.1	L	SN	90.	−7.	−0.079	0.120	0.357	0.621
25		05/16 0601 (136) 05/16 0601	7.42	F_r	490.3	L	NSN	300.	23.	−0.018	0.041	0.247	0.855
26		05/26 0909 (146) 05/26 1535	32.42	F_r	330.5	R	SNS	256.	−50.	−0.047	0.130	0.340	0.219
27		06/08 1543 (159) 06/09 0618	16.73	F_r	373.8	R	SN	233.	−5.	−0.035	0.068	0.261	0.704
28		06/19 0000 (170) 06/19 0531	40.98	F_r	332.5	R	SN	311.	−7.	0.143	0.187	0.328	0.479
29		07/15 0310 (196) 07/15 0648	28.47	F^+	359.2	L	SNS	115.	−30.	−0.028	0.112	0.359	0.662
30		08/03 1010 (215) 08/03 1355	12.47	F_r	437.2	L	SN	43.	−4.	−0.038	0.055	0.202	0.679
31		08/17 0156 (229) 08/17 0633	13.60	F_r	396.2	R	S	78.	−32.	−0.037	0.067	0.597	0.238
32		09/02 2240 (245) 09/03 0838	12.35	F_r	408.8	R	NS	56.	12.	0.036	0.058	0.340	0.331
33		09/18 0030 (261) 09/18 0407	43.88	F^+	320.3	R	SNN	227.	37.	0.064	0.152	0.410	0.436
34		09/21 1642 (264) 09/21 2221	19.43	F^+	423.5	L	N	51.	61.	−0.083	0.124	0.266	0.448
35		10/01 1145 (274) 10/01 1708	30.13	F_r	450.5	L	N	172.	22.	0.094	0.113	0.301	0.284
36		10/10 0308 (283) 10/10 1533	30.45	F^+	410.2	R	SNS	220.	−45.	0.052	0.131	0.358	0.698
37		11/06 2225 (310) 11/07 0600	40.78	F^+	412.7	R	SNN	228.	45.	0.017	0.175	0.367	0.688
38		11/22 0912 (326) 11/22 1731	25.20	F^+	499.6	R	S	191.	−69.	0.041	0.141	0.368	0.404
39		12/10 0433 (344) 12/10 1911	28.82	C_x										
40		12/30 0113 (364) 12/30 0935	23.28	F_r	366.2	L	SN	52.	14.	−0.019	0.080	0.530	0.491
41	1998	01/06 1329 (6) 01/07 0223	29.53	F^+	383.3	L	SNN	30.	44.	0.001	0.104	0.204	0.765
42		01/08 1535 (8) 01/08 1535	7.20	F^-	370.8	R	SNN	275.	16.	−0.020	0.037	0.299	0.754

Table 5 (*Continued*)

E	Year	ICME$_s$ (DOY) MO$_s$	ΔT_{MO} hrs	MO	V_{sw} kms^{-1}	H	Conf.	ϕ (°)	θ (°)	y_0 (AU)	R (AU)	χ^2	ρ
43		01/09 0823 (9) 01/09 0823	12.25	F_r	476.5	L	SN	87.	−18.	−0.071	0.098	0.216	0.599
44		01/21 0447 (21) 01/21 0447	32.65	F^-	410.3	R	N	3.	17.	0.079	0.091	0.344	0.450
45		01/28 1604 (28) 01/29 1312	34.80	F^+	376.7	R	S	313.	−65.	−0.017	0.148	0.388	0.413
46		02/02 1027 (33) 02/02 1027	39.93	F^+	335.3	L	NS	248.	10.	0.167	0.222	0.406	0.155
47		02/04 0448 (35) 02/04 0448	51.28	F^+	320.1	L	N	40.	24.	0.413	0.435	0.504	0.614
48		02/17 0628 (48) 02/17 1048	27.58	F_r	397.0	R	SNS	307.	−48.	0.017	0.115	0.346	0.543
49		02/18 1452 (49) 02/18 2135	27.15	F_r	436.3	L	NS	271.	2.	0.072	0.154	0.301	0.535
50		03/04 1102 (63) 03/04 1048	44.38	F^+	347.8	L	SN	106.	11.	−0.028	0.175	0.291	0.817
51		03/06 1159 (65) 03/06 1159	28.82	C_x									
52		03/25 1048 (84) 03/25 1423	18.58	F_r	406.6	L	SN	103.	4.	−0.016	0.087	0.414	0.668
53		03/31 0711 (90) 03/31 1159	28.33	F_r	389.2	R	S	43.	−49.	−0.393	0.409	0.256	0.433
54		04/01 2107 (91) 04/01 2107	22.80	E									
55		05/01 2121 (121) 05/02 1131	29.28	F_r	517.2	L	SNN	10.	21.	0.102	0.123	0.303	0.673
56		05/04 0230 (124) 05/04 0950	17.37	F^-	651.4	R	S	105.	−22.	−0.348	0.369	0.388	0.118
57		06/02 1028 (153) 06/02 1024	8.80	F_r	398.9	L	SNN	134.	23.	0.035	0.046	0.338	0.593
58		06/24 1047 (175) 06/24 1326	33.12	F^+	468.2	L	SNN	149.	28.	0.016	0.122	0.230	0.729
59		07/10 2236 (191) 07/10 2236	46.98	F^+	387.1	L	SN	106.	−2.	−0.345	0.401	0.492	0.487
60		08/10 0031 (222) 08/10 0447	18.73	E									
61		08/19 1840 (231) 08/20 0838	35.52	F^+	317.4	R	SN	298.	3.	0.033	0.119	0.418	0.657
62		08/26 0640 (238) 08/26 2107	27.35	E									
63		09/23 0112 (266) 09/23 0419	13.20	F^-	413.0	L	NS	219.	19.	−0.052	0.068	0.332	0.572
64		09/24 2318 (267) 09/25 0433	36.45	F^+	660.5	L	NSN	197.	39.	−0.094	0.207	0.376	0.607
65		10/02 0710 (275) 10/02 0710	15.62	E									
66		10/18 1930 (291) 10/19 0419	26.87	F^+	395.7	L	SN	104.	−24.	0.035	0.125	0.296	0.596

Table 5 (*Continued*)

E	Year	ICME$_s$ (DOY) MO$_s$	ΔT_{MO} hrs	MO	V_{sw} km s^{-1}	H	Conf.	ϕ (°)	θ (°)	y_0 (AU)	R (AU)	χ^2	ρ
67		10/23 1257 (296) 10/23 1955	23.52	F^-	495.1	R	NS	131.	−5.	−0.637	0.645	0.342	0.381
68		11/08 0441 (312) 11/08 0441	18.83	C_x									
69		11/09 0044 (313) 11/09 0044	27.05	F^+	437.6	R	S	346.	−77.	−0.022	0.135	0.293	0.506
70	1999	01/22 2021 (22) 01/22 2021	18.63	E									
71		02/11 1741 (42) 02/11 1741	9.90	F_r	442.4	R	NSN	113.	36.	−0.005	0.048	0.448	0.474
72		02/18 0248 (49) 02/18 0914	14.77	E									
73		04/16 1114 (106) 04/16 1911	24.62	F_r	328.0	L	SNS	137.	−41.	−0.029	0.084	0.327	0.910
74		04/21 1237 (111) 04/21 1237	49.77	E									
75		05/28 2150 (148) 05/28 2150	36.95	C_x									
76		06/26 0231 (177) 06/26 0231	26.27	F_r	290.8	L	SN	92.	−5.	−0.026	0.091	0.382	0.436
77		07/02 0027 (183) 07/03 0809	53.08	F_r	458.0	R	SNS	264.	−17.	−0.555	0.624	0.311	0.487
78		07/06 1423 (187) 07/06 1912	21.58	C_x									
79		07/30 1912 (211) 07/31 0202	21.97	E									
80		08/06 0155 (218) 08/06 1423	15.92	F_r	265.5	L	SN	27.	−10.	−0.048	0.053	0.207	0.341
81		08/09 1012 (221) 08/09 1012	29.87	F_r	343.6	L	N	124.	67.	−0.037	0.122	0.306	0.425
82		09/15 0743 (258) 09/15 0743	10.03	E									
83		09/21 1857 (264) 09/21 1857	16.57	F_r	358.4	L	SNN	79.	12.	−0.090	0.113	0.403	0.395
84		09/22 1209 (265) 09/22 1759	15.60	E									
85		10/21 0219 (294) 10/21 0219	28.23	E									
86		11/13 1248 (317) 11/14 1423	40.90	E									
87		12/12 1550 (346) 12/12 1731	24.95	C_x									
88	2000	02/11 2334 (42) 02/12 1220	12.25	F_r	549.1	R	NSN	178.	15.	0.006	0.022	0.309	0.386
89		02/14 0711 (45) 02/14 1311	26.38	E									

Table 5 (*Continued*)

E	Year	ICME$_s$ (DOY) MO$_s$	ΔT_{MO} hrs	MO	V_{sw} km s^{-1}	H	Conf.	ϕ (°)	θ (°)	$y0$ (AU)	R (AU)	χ^2	ρ
90		02/20 2103 (51) 02/21 1424	22.88	F_r	379.4	R	N	233.	97.	0.051	0.112	0.344	0.481
91		03/01 0158 (61) 03/01 0321	23.77	F_r	474.2	L	NSN	351.	51.	0.238	0.259	0.303	0.128
92		03/28 0252 (88) 03/28 0252	43.93	E										
93		05/07 0353 (128) 05/07 0353	32.10	C_x										
94		06/08 0907 (160) 06/08 1647	32.53	E										
95		06/23 1257 (175) 06/24 0900	38.98	E										
96		07/01 0712 (183) 07/01 0712	20.38	F_r	412.7	L	N	19.	75.	0.062	0.114	0.306	0.718
97		07/11 2235 (193) 07/11 2235	29.97	F_r	507.7	L	SNN	156.	26.	0.014	0.102	0.320	0.771
98		07/13 0959 (195) 07/13 1535	24.00	F_r	450.0	L	NSS	250.	-35.	-0.339	0.359	0.387	0.234
99		07/15 0223 (197) 07/15 0647	7.53	F^-	500.0	L	S	225.	-57.	0.089	0.097	0.238	0.510
100		07/15 1423 (197) 07/15 1731	19.95	F^+	900.0	L	SNN	47.	22.	-0.036	0.154	0.365	0.671
101		07/19 1530 (201) 07/19 1530	38.02	C_x										
102		07/28 0638 (210) 07/28 1424	19.70	F^+	462.6	L	NSN	338.	37.	0.032	0.078	0.339	0.633
103		07/31 2328 (213) 07/31 2328	13.73	F_r	455.8	R	NS	62.	6.	0.206	0.215	0.240	-0.019
104		08/10 0513 (223) 08/10 2052	21.85	F^+	422.9	L	SNS	162.	-14.	0.054	0.068	0.219	0.488
105		08/11 1849 (224) 08/12 0605	23.00	F^+	579.1	L	SN	105.	13.	0.023	0.149	0.275	0.481
106		09/02 2316 (246) 09/02 2316	23.28	F_r	408.5	R	NSN	53.	62.	0.105	0.151	0.263	0.475
107		09/04 1313 (248) 09/04 1313	51.57	C_x										
108		09/06 1702 (250) 09/07 0324	34.98	C_x										
109		09/17 1604 (261) 09/18 0153	34.12	E										
110		10/03 0102 (277) 10/03 0936	41.98	F^+	408.1	R	NS	52.	2.	0.022	0.159	0.598	0.532
111		10/05 0328 (279) 10/05 1911	24.48	F_r	475.3	R	SN	261.	-11.	0.072	0.153	0.475	0.379
112		10/12 2233 (286) 10/13 1824	24.80	F_r	400.9	L	NS	184.	4.	-0.011	0.016	0.196	0.786
113		10/28 0638 (302) 10/28 2318	24.98	F^-	383.2	L	SNS	123.	-20.	0.054	0.109	0.340	0.399

Table 5 (*Continued*)

E	Year	ICME$_s$ (DOY) MO$_s$	ΔT_{MO} hrs	MO	V_{sw} km s^{-1}	H	Conf.	ϕ (°)	θ (°)	y_0 (AU)	R (AU)	χ^2	ρ
114		11/06 0930 (311) 11/06 2305	19.00	F_r	536.9	L	SN	119.	9.	0.030	0.106	0.217	0.723
115		11/10 0620 (315) 11/10 1102	17.28	E									
116		11/11 0411 (316) 11/11 0411	19.80	E									
117		11/26 1143 (331) 11/27 0930	24.10	F_r	574.8	L	NSS	183.	−62.	0.086	0.170	0.249	0.598
118		12/03 0359 (338) 12/03 0359	47.13	C_x									
119	2001	01/23 1047 (23) 01/24 0838	34.57	C_x									
120		03/04 0545 (63) 03/04 0545	41.33	C_x									
121		03/19 1133 (78) 03/19 1955	22.37	F_r	419.2	L	NSS	224.	−47.	0.002	0.092	0.313	0.555
122		03/20 1817 (79) 03/20 1815	29.73	F_r	340.4	L	SN	155.	−6.	0.083	0.098	0.236	0.186
123		03/27 0159 (86) 03/27 0159	36.40	C_x									
124		04/04 1439 (94) 04/04 2054	11.48	F^-	738.5	L	NS	272.	15.	0.165	0.192	0.250	0.453
125		04/11 1409 (101) 04/11 2248	19.18	F^-	662.6	R	SN	321.	20.	0.088	0.131	0.279	0.310
126		04/13 0726 (103) 04/13 1311	12.48	F^-	763.4	R	SN	337.	7.	0.152	0.158	0.283	0.015
127		04/21 1529 (111) 04/22 0028	24.72	F_r	358.6	L	NSS	271.	−55.	−0.006	0.103	0.210	0.608
128		04/28 0500 (118) 04/28 1759	82.82	C_x									
129		05/27 1445 (147) 05/28 0712	38.38	C_x									
130		06/27 0559 (178) 06/27 0559	44.40	C_x									
131		08/05 1228 (217) 08/06 0643	17.27	E									
132		08/17 1101 (229) 08/17 2359	19.22	F^-	534.0	R	S	154.	−29.	0.255	0.265	0.251	0.213
133		09/25 2016 (268) 09/26 1004	6.73	F^-	430.4	R	S	123.	−33.	0.087	0.092	0.213	0.770
134		09/29 0928 (272) 09/29 1423	28.85	C_x									
135		09/30 1914 (273) 09/30 2233	23.03	F^-	505.0	R	NSS	55.	−60.	0.087	0.154	0.391	0.280
136		10/02 2324 (275) 10/02 2324	17.13	F_r	508.1	L	S	217.	−71.	0.013	0.101	0.468	0.707

Table 5 (*Continued*)

E	Year	ICME$_s$ (DOY) MO$_s$	ΔT_{MO} hrs	MO	V_{sw} km s^{-1}	H	Conf.	ϕ (°)	θ (°)	y_0 (AU)	R (AU)	χ^2	ρ
137		10/21 1639 (294) 10/22 0117	23.50	F_r	579.4	L	S	165.	−31.	−0.009	0.090	0.459	0.695
138		10/28 0313 (301) 10/29 1619	18.47	E									
139		10/31 1346 (304) 10/31 2204	30.72	F_r	340.7	L	SN	117.	−6.	0.037	0.116	0.324	0.189
140		11/24 0551 (328) 11/24 1547	21.50	F_r	745.1	L	N	106.	78.	0.150	0.233	0.452	0.305
141		12/29 0516 (363) 12/30 0324	15.78	F_r	400.6	L	N	261.	52.	0.074	0.103	0.615	0.456
142		12/30 2005 (364) 12/30 2310	8.60	F^-	523.5	R	SN	217.	10.	−0.217	0.219	0.266	0.160
143	2002	02/28 0506 (59) 02/28 1911	28.08	F_r	369.8	R	SNN	342.	24.	−0.030	0.068	0.440	0.461
144		03/18 1314 (77) 03/19 0614	33.37	F_r	384.7	R	NSN	105.	59.	−0.042	0.157	0.233	0.657
145		03/23 1124 (82) 03/24 1311	32.42	F_r	436.6	R	SNN	309.	40.	0.020	0.149	0.216	0.865
146		04/14 1256 (104) 04/14 1521	13.02	F^-	397.1	L	N	38.	36.	−0.205	0.210	0.266	0.323
147		04/17 1101 (107) 04/17 2136	34.78	F^+	488.5	R	SNS	302.	−21.	0.110	0.201	0.290	0.747
148		04/19 0824 (109) 04/20 0657	38.65	F_r	505.4	L	SN	153.	−9.	0.031	0.112	0.380	0.410
149		04/23 0500 (113) 04/24 0711	16.80	F^-	490.4	R	NS	35.	−4.	0.765	0.767	0.341	0.107
150		05/10 1109 (130) 05/10 2220	12.27	F_r	356.3	R	NSN	34.	32.	−0.056	0.067	0.321	0.405
151		05/11 1030 (131) 05/11 1237	7.77	F_r	436.6	R	S	353.	−78.	0.004	0.039	0.435	0.535
152		05/18 1945 (138) 05/19 0330	24.07	F_r	455.7	R	SN	235.	−5.	0.332	0.349	0.278	0.300
153		05/20 0335 (140) 05/20 1647	28.80	C_x									
154		05/23 1044 (143) 05/23 2302	44.17	F^-	550.3	L	SNN	57.	14.	−1.705	1.722	0.224	0.178
155		07/17 1556 (198) 07/18 1326	20.15	F_r	396.7	L	N	19.	64.	−0.086	0.122	0.408	0.408
156		08/01 0512 (213) 08/01 1214	11.03	F_r	454.0	R	SN	263.	12.	0.019	0.062	0.315	0.579
157		08/01 2309 (213) 08/02 0712	14.38	F_r	491.9	L	NS	230.	−10.	0.009	0.064	0.294	0.697
158		08/18 1840 (230) 08/19 1912	42.23	F_r	449.1	L	NSS	184.	−16.	0.086	0.107	0.545	0.275
159		08/26 1116 (238) 08/26 1423	20.40	F_r	397.8	R	SNS	249.	−27.	−0.170	0.193	0.358	0.182
160		09/03 0223 (246) 09/03 0447	20.43	C_x									

Table 5 (*Continued*)

E	Year	ICME$_s$ (DOY) MO$_s$	ΔT_{MO} hrs	MO	V_{sw} km s^{-1}	H	Conf.	ϕ (°)	θ (°)	y_0 (AU)	R (AU)	χ^2	ρ
161		09/30 0754 (273) 09/30 2204	22.08	F^+	380.7	R	NS	109.	−3.	0.023	0.094	0.339	0.758
162		11/16 2316 (320) 11/17 2024	27.58	F^-	383.5	L	SN	14.	15.	0.216	0.220	0.275	0.261
163		12/21 0321 (355) 12/21 1020	29.27	F_r	429.7	R	SN	284.	34.	0.139	0.202	0.306	0.591
164	2003	01/26 2143 (26) 01/27 0140	14.40	F_r	519.3	R	N	3.	52.	−0.009	0.065	0.367	0.741
165		02/01 1306 (32) 02/02 1911	14.40	F_r	482.6	L	SNN	15.	31.	0.031	0.055	0.286	0.603
166		03/20 0430 (79) 03/20 1154	10.48	F_r	671.9	L	S	202.	−77.	−0.077	0.110	0.162	0.706
167		05/09 0516 (129) 05/09 0927	37.68	E									
168		06/16 2233 (167) 06/17 1748	14.50	F_r	480.7	L	NS	213.	−11.	0.041	0.059	0.274	0.550
169		08/04 2023 (216) 08/05 0110	25.22	F_r	442.6	R	NS	12.	−5.	−0.026	0.038	0.397	0.443
170		10/21 2200 (294) 10/22 0224	48.00	C_x									
171		10/29 0600 (302) 10/29 1116	14.65	C_x									
172		10/30 1612 (303) 10/31 0200	10.00	C_x									
173		11/20 0835 (324) 11/20 1131	14.15	F_r	588.2	R	S	167.	−78.	0.007	0.090	0.352	0.548
174	2004	01/09 1500 (9) 01/10 0601	23.02	E									
175		04/03 0955 (94) 04/04 0111	42.00	F^+	431.8	L	N	341.	68.	0.066	0.210	0.404	0.664
176		07/22 0945 (204) 07/22 1326	40.32	C_x									
177		07/24 0532 (206) 07/24 0712	31.43	F_r	548.0	R	NS	82.	−31.	0.057	0.210	0.289	0.534
178		07/25 1745 (207) 07/25 1745	9.83	F_r	577.9	R	S	182.	−47.	−0.004	0.049	0.382	0.696
179		07/26 2225 (208) 07/27 0112	22.78	C_x									
180		08/29 0909 (242) 08/29 1926	25.92	F_r	393.6	R	NS	58.	−16.	−0.014	0.103	0.227	0.759
181		09/13 1942 (257) 09/14 1759	20.40	E									
182		09/17 2052 (261) 09/18 1228	28.50	F_r	402.5	R	N	−9.	37.	0.052	0.098	0.484	0.177
183		11/07 1758 (312) 11/07 2246	34.58	F_r	639.7	L	SN	136.	−11.	0.133	0.223	0.429	0.290

Table 5 (*Continued*)

E	Year	ICME$_s$ (DOY) MO$_s$	ΔT_{MO} hrs	MO	V_{sw} km s^{-1}	H	Conf.	ϕ (°)	θ (°)	y_0 (AU)	R (AU)	χ^2	ρ
184		11/09 1825 (314) 11/09 2038	20.15	F^+	729.2	L	NSS	232.	−58.	−0.047	0.164	0.532	0.368
185		11/11 1647 (316) 11/12 0835	25.00	F_r	550.1	L	S	328.	−80.	0.171	0.232	0.358	0.462
186		12/10 0447 (345) 12/10 0447	16.80	F^-	417.2	R	NS	164.	−1.	−0.057	0.062	0.511	0.042
187	2005	01/07 0844 (7) 01/07 1423	16.82	F^+	536.3	L	SNS	26.	−35.	0.017	0.072	0.695	0.328
188		01/08 1512 (8) 01/08 2051	20.90	F_r	461.6	L	N	21.	64.	−0.094	0.138	0.368	0.524
189		01/16 0927 (16) 01/16 1535	15.43	F^+	529.3	L	NSS	273.	−28.	−0.105	0.137	0.574	0.507
190		01/18 2135 (18) 01/19 0028	25.93	F^-	829.6	R	NSS	158.	−10.	−0.031	0.104	0.415	0.135
191		01/21 1658 (21) 01/21 2345	19.45	F^-	269.3	L	NS	250.	−2.	0.111	0.124	0.320	0.219
192		02/16 1033 (47) 02/16 1214	11.28	F^-	390.7	R	SN	313.	−5.	−0.006	0.038	0.519	0.392
193		02/17 2135 (48) 02/18 1452	17.52	E									
194		02/20 1532 (51) 02/20 2023	34.80	F_r	409.8	R	SN	−6.	1.	0.019	0.026	0.331	0.363
195		05/15 0210 (135) 05/15 0531	41.27	F^+	745.8	R	SN	265.	−6.	0.640	0.732	0.433	0.034
196		05/20 0447 (140) 05/20 0935	40.80	F^+	427.5	L	NS	238.	−12.	−0.025	0.172	0.476	0.468
197		06/12 0657 (163) 06/12 1507	26.88	F^-	480.3	L	SNS	147.	−28.	0.095	0.138	0.315	0.520
198		06/14 1755 (165) 06/15 0508	27.25	F^+	484.0	L	SNN	69.	31.	−0.024	0.145	0.460	0.369
199		07/10 0242 (191) 07/10 1047	51.60	C_x									
200		07/17 1452 (198) 07/17 1452	15.13	F_r	426.4	R	NSS	40.	−29.	−0.002	0.054	0.321	0.749
201		08/10 0447 (222) 08/10 0614	7.20	F^-	446.9	R	S	11.	−12.	0.068	0.068	0.341	0.384
202		10/31 0223 (304) 10/31 0223	16.33	F_r	373.8	R	NS	156.	−6.	−0.005	0.030	0.305	0.745
203	2006	02/05 1814 (36) 02/05 2023	15.60	F^+	341.4	R	NSS	94.	−37.	−0.005	0.062	0.303	0.683
204		04/13 1326 (103) 04/13 1507	19.92	F^+	521.2	L	NS	283.	12.	−0.001	0.116	0.326	0.776
205		04/14 1311 (104) 04/14 1311	10.08	F^-	514.9	R	SN	206.	−5.	−0.103	0.106	0.301	0.523
206		06/14 0809 (165) 06/14 0809	8.28	F^-	385.7	L	SNN	72.	3.	−0.191	0.194	0.319	0.199

Table 5 (*Continued*)

E	Year	ICME$_s$ (DOY) MO$_s$	ΔT_{MO} hrs	MO	V_{sw} km s^{-1}	H	Conf.	ϕ (°)	θ (°)	y_0 (AU)	R (AU)	χ^2	ρ
207		07/09 2040 (190) 07/10 1745	24.00	C_x									
208		08/19 0938 (231) 08/20 1355	27.12	C_x									
209		08/30 2038 (242) 08/30 2038	34.57	C_x									
210		09/30 0252 (273) 09/30 0823	13.68	F^+	394.2	L	NS	269.	19.	−0.010	0.062	0.594	0.555
211		11/01 2121 (305) 11/01 2121	17.03	F^-	374.2	R	NS	11.	−1.	0.038	0.040	0.355	0.299
212		11/18 0711 (322) 11/18 0711	45.60	F_r	399.6	R	SN	343.	2.	0.121	0.137	0.323	0.486
213		11/29 0258 (333) 11/29 0516	28.32	F^+	254.9	R	NS	58.	18.	−0.003	0.074	0.361	0.772
214		12/14 1351 (348) 12/14 2236	15.07	F^-	752.5	L	S	163.	−21.	0.431	0.435	0.334	−0.131
215		12/16 1734 (350) 12/17 0025	18.77	F^-	585.7	L	N	146.	84.	0.922	0.931	0.204	0.442
216	2007	01/14 1131 (14) 01/14 1144	20.02	F_r	363.8	L	NS	286.	6.	0.039	0.089	0.294	0.702
217		01/15 2049 (15) 01/15 2049	7.93	F^-	534.4	R	NSS	82.	−21.	0.128	0.137	0.438	−0.099
218		03/29 1504 (88) 03/29 1504	8.98	C_x									
219		05/21 2240 (141) 05/21 2245	14.67	F_r	454.6	R	NSN	25.	41.	0.000	0.051	0.283	0.769
220		06/08 0545 (159) 06/08 0545	23.50	F_r	362.4	L	NS	318.	−4.	−0.029	0.070	0.507	−0.216
221		11/19 1722 (323) 11/20 0033	10.97	F_r	465.3	L	NS	279.	−8.	0.006	0.058	0.400	0.607
222		12/25 1619 (359) 12/25 1619	17.27	F^-	350.1	R	SN	262.	1.	0.085	0.110	0.403	0.313
223	2008	05/23 0112 (144) 05/23 0112	9.58	F^+	499.6	R	NSN	65.	42.	−0.047	0.071	0.255	0.771
224		09/03 1633 (247) 09/03 1633	11.28	F^+	467.0	R	NS	81.	6.	−0.029	0.067	0.274	0.346
225		09/17 0043 (261) 09/17 0357	28.20	F_r	408.3	R	N	43.	61.	−0.062	0.138	0.310	0.585
226		12/04 1159 (339) 12/04 1647	18.00	F_r	390.1	R	NSS	117.	−21.	0.019	0.075	0.505	0.345
227		12/17 0335 (352) 12/17 0335	12.00	F_r	336.6	L	NSS	234.	−18.	0.023	0.043	0.290	0.588
228	2009	01/02 0249 (2) 01/02 0448	12.47	F^-	410.5	R	NSN	86.	16.	0.112	0.124	0.387	0.354
229		01/26 0502 (26) 01/26 0502	10.32	E									

Table 5 (*Continued*)

E	Year	ICME$_s$ (DOY) MO$_s$	ΔT_{MO} hrs	MO	V_{sw} km s^{-1}	H	Conf.	ϕ (°)	θ (°)	y_0 (AU)	R (AU)	χ^2	ρ
230		02/03 1921 (34) 02/04 0112	18.47	F^+	356.7	R	NSS	122.	−67.	0.006	0.076	0.520	0.458
231		03/11 2204 (70) 03/12 0112	24.47	F^+	361.1	R	NSN	86.	41.	−0.018	0.105	0.350	0.196
232		04/05 1604 (95) 04/05 1702	11.77	F^-	403.6	R	NSS	155.	−18.	0.008	0.029	0.396	0.496
233		04/22 1116 (112) 04/22 1409	6.48	F_r	387.9	R	NS	82.	6.	0.007	0.029	0.368	0.515
234		06/03 1340 (154) 06/03 2052	32.65	F_r	315.6	L	NS	206.	−16.	0.087	0.106	0.284	0.329
235		06/27 1102 (178) 06/27 1759	26.42	F^+	388.4	R	NSN	70.	41.	−0.001	0.112	0.482	0.462
236		07/21 0253 (202) 07/21 0448	22.80	F_r	316.6	R	NS	135.	−29.	−0.029	0.072	0.230	0.420
237		09/10 1019 (253) 09/10 1019	9.12	F_r	305.4	R	NS	141.	13.	−0.025	0.032	0.322	0.402
238		09/30 0044 (273) 09/30 0659	12.20	F_r	346.5	L	NSN	306.	22.	−0.007	0.039	0.194	0.918
239		10/29 0126 (302) 10/29 0126	22.32	F^+	364.1	L	NS	266.	16.	−0.015	0.097	0.331	0.583
240		11/01 1004 (305) 11/01 1004	22.28	F^-	347.7	L	NSN	211.	11.	0.118	0.127	0.274	0.221
241		11/14 1047 (318) 11/14 1047	24.97	F_r	334.8	R	SN	337.	−7.	0.041	0.056	0.535	0.141
242		12/12 0447 (346) 12/12 1926	33.35	F_r	271.0	R	NS	60.	−7.	0.079	0.122	0.288	0.527
243	2010	01/01 2204 (1) 01/02 0014	32.88	F_r	286.3	R	NS	63.	23.	0.017	0.101	0.288	0.662
244		02/07 1804 (38) 02/07 1911	34.52	F_r	361.7	R	N	198.	17.	−0.124	0.139	0.424	0.602
245		03/23 2229 (82) 03/23 2233	17.05	F_r	292.6	R	NS	49.	−10.	0.075	0.086	0.274	0.521
246		04/05 0755 (95) 04/05 1159	28.82	F_r	634.3	R	NS	12.	5.	−0.045	0.066	0.240	0.665
247		04/11 1220 (101) 04/11 2136	16.60	F_r	411.2	R	SN	199.	8.	−0.034	0.043	0.231	0.771
248		05/18 0223 (138) 05/18 0404	27.37	F_r	355.0	R	SN	292.	28.	0.013	0.105	0.281	0.634
249		05/28 0155 (148) 05/28 1912	22.78	F_r	354.0	L	S	254.	−68.	−0.008	0.093	0.276	0.687
250		06/21 0335 (172) 06/21 0628	30.25	F_r	361.7	R	NSN	79.	34.	0.036	0.133	0.542	0.300
251		08/03 1705 (215) 08/04 0252	22.08	C_x									
252		09/15 0224 (258) 09/15 0224	33.58	F_r	370.8	R	SNN	282.	20.	−0.030	0.147	0.719	−0.052
253		09/25 1145 (268) 09/25 1311	18.97	F^-	473.7	L	NSS	315.	−17.	0.017	0.078	0.374	0.489

Table 5 (*Continued*)

E	Year	ICME$_s$ (DOY) MO$_s$	ΔT_{MO} hrs	MO	V_{sw} km s^{-1}	H	Conf.	ϕ (°)	θ (°)	y_0 (AU)	R (AU)	χ^2	ρ
254		10/11 0545 (284) 10/11 0545	12.72	F^-	354.0	R	S	81.	−74.	0.071	0.085	0.516	0.139
255		10/31 0209 (304) 10/31 0516	39.37	F_r	341.7	R	N	342.	59.	0.000	0.139	0.364	0.571
256		12/19 2035 (353) 12/19 2233	23.52	F^+	385.0	L	S	80.	−48.	−0.060	0.118	0.736	0.271
257	2011	01/24 0643 (24) 01/24 1033	35.52	F^+	343.1	R	NSS	173.	−19.	−0.014	0.051	0.363	0.533
258		02/18 1950 (49) 02/18 1955	49.67	F^-	461.4	L	NS	304.	−10.	−0.720	0.755	0.507	−0.070
259		03/29 1512 (88) 03/29 2359	62.88	F_r	344.4	R	NS	135.	1.	−0.060	0.191	0.383	0.404
260		04/23 0001 (113) 04/23 0001	37.17	F^-	397.7	L	SN	42.	−1.	−0.336	0.355	0.355	0.439
261		04/29 0907 (119) 04/29 1355	6.95	E									
262		05/28 0014 (148) 05/28 0531	17.28	F^+	520.8	R	SN	268.	8.	0.013	0.101	0.702	0.420
263		06/04 2006 (155) 06/05 0112	17.03	F_r	513.7	R	NS	119.	34.	0.006	0.090	0.333	0.690
264		06/17 0209 (168) 06/17 0516	49.93	C_x									
265		06/30 1326 (181) 06/30 1843	10.55	F^-	329.3	L	NSS	218.	−33.	0.068	0.075	0.251	0.548
266		07/03 1912 (184) 07/03 1912	24.00	F_r	391.6	L	NS	236.	−10.	0.120	0.150	0.278	0.203
267		09/17 0257 (260) 09/17 1535	29.53	F_r	443.1	L	SNN	162.	24.	0.160	0.176	0.512	0.021
268		10/05 0646 (278) 10/05 0956	40.17	C_x									
269		10/24 1741 (297) 10/25 0021	23.17	C_x									
270		11/01 0809 (305) 11/01 0809	13.92	F^-	411.2	R	NS	43.	5.	0.056	0.071	0.451	0.233
271		11/02 0021 (306) 11/02 0335	24.97	F_r	371.0	L	SN	108.	−7.	0.021	0.104	0.513	0.403
272		11/04 2027 (308) 11/04 2117	22.87	C_x									
273		11/07 0657 (311) 11/07 1619	8.40	F_r	348.9	L	NS	212.	−2.	0.090	0.092	0.251	0.518
274		11/11 0301 (315) 11/11 0301	26.02	C_x									
275		11/28 2059 (332) 11/29 1940	22.32	C_x									
276	2012	01/21 0402 (21) 01/21 0404	26.88	F_r	327.0	R	SN	304.	21.	0.030	0.092	0.187	0.725

Table 5 (*Continued*)

E	Year	ICME$_s$ (DOY) MO$_s$	ΔT_{MO} hrs	MO	V_{sw} kms^{-1}	H	Conf.	ϕ (°)	θ (°)	$y0$ (AU)	R (AU)	χ^2	ρ
277		01/22 0533 (22) 01/22 1124	6.58	F^-	411.5	R	NS	28.	1.	-0.028	0.032	0.219	0.328
278		02/14 0711 (45) 02/14 2052	31.93	F_r	377.7	R	SNS	274.	-30.	-0.011	0.141	0.318	0.555
279		02/26 2059 (57) 02/27 1759	59.77	C_x									
280		03/08 1032 (68) 03/08 1955	59.52	C_x									
281		03/12 0828 (72) 03/12 1619	34.55	C_x									
282		03/15 1235 (75) 03/15 1604	22.10	F_r	697.3	R	SNS	290.	-51.	-0.069	0.185	0.400	0.618
283		04/05 1423 (96) 04/05 1941	25.92	F_r	341.3	R	N	149.	60.	0.033	0.098	0.324	0.657
284		04/11 0628 (102) 04/11 0628	21.13	C_x									
285		04/23 0215 (114) 04/23 1648	10.07	F^-	373.0	R	SNS	205.	-25.	-0.042	0.048	0.291	0.334
286		05/03 0059 (124) 05/04 0336	31.78	F_r	310.0	L	NS	217.	3.	-0.167	0.180	0.278	0.431
287		05/16 1228 (137) 05/16 1604	34.12	F_r	374.0	R	SNN	229.	29.	-0.049	0.131	0.469	0.390
288		06/11 0252 (163) 06/11 1131	17.75	F_r	408.9	L	S	301.	-76.	0.013	0.079	0.396	0.399
289		06/16 0903 (168) 06/16 2201	13.37	F^+	451.1	R	NS	106.	-4.	-0.004	0.063	0.298	0.664
290		07/08 0210 (190) 07/08 0758	41.73	C_x									
291		07/14 1739 (196) 07/15 0614	45.13	F_r	492.0	R	S	0.	-7.	0.042	0.053	0.403	0.084
292		08/12 1237 (225) 08/12 1912	9.83	F_r	382.0	L	NS	348.	3.	-0.015	0.018	0.260	0.604
293		08/18 0325 (231) 08/18 1912	13.18	F_r	386.1	R	NS	3.	5.	0.008	0.010	0.292	0.509
294		08/30 1535 (243) 08/30 1535	13.93	F^-	404.6	R	SNS	275.	-13.	-0.061	0.088	0.338	0.633
295		09/01 0712 (245) 09/01 0712	52.18	F_r	317.2	R	NSS	145.	-21.	-0.152	0.196	0.311	0.366
296		09/04 2202 (248) 09/05 0552	11.88	F_r	506.2	L	SNN	45.	51.	-0.081	0.102	0.293	0.135
297		09/06 0000 (250) 09/06 0223	13.45	F^-	425.8	L	NSN	203.	13.	0.098	0.102	0.270	0.478
298		09/12 1955 (256) 09/12 1955	19.43	F^-	364.9	L	SNS	31.	-1.	0.659	0.661	0.422	0.104
299		09/30 1014 (274) 09/30 1214	38.65	C_x									
300		10/08 0412 (282) 10/08 1550	25.45	F_r	397.5	R	S	272.	-79.	-0.032	0.119	0.410	0.467

Table 5 (*Continued*)

E	Year	ICME$_s$ (DOY) MO$_s$	ΔT_{MO} hrs	MO	V_{sw} km s^{-1}	H	Conf.	ϕ (°)	θ (°)	y_0 (AU)	R (AU)	χ^2	ρ
301		10/12 0809 (286) 10/12 1829	14.75	F_r	481.0	L	S	281.	−65.	−0.048	0.094	0.238	0.329
302		10/31 1428 (305) 10/31 2335	29.77	F^+	340.8	R	S	355.	−78.	−0.006	0.112	0.365	0.499
303		11/12 2212 (317) 11/13 0823	23.77	F^+	381.8	R	NS	90.	−17.	0.010	0.106	0.275	0.533
304		11/23 2051 (328) 11/24 1131	23.27	F^-	380.8	R	SNN	206.	12.	−0.094	0.105	0.320	0.202
305	2013	01/16 2331 (16) 01/17 1452	21.37	F_r	387.2	R	SN	281.	5.	0.023	0.094	0.308	0.708
306		01/18 2247 (18) 01/19 0014	16.55	F_r	427.4	L	S	184.	−29.	−0.047	0.062	0.231	0.820
307		01/19 1650 (19) 01/19 2247	12.00	F^-	428.2	R	S	5.	−12.	0.050	0.052	0.378	0.407
308		03/17 0521 (76) 03/17 1409	49.92	F_r	528.9	R	N	249.	65.	−0.358	0.472	0.491	0.257
309		04/13 2213 (103) 04/14 1702	60.48	F^+	389.8	L	NS	265.	23.	0.039	0.283	0.513	0.551
310		04/30 0852 (120) 04/30 1200	19.20	F_r	392.8	L	NS	311.	8.	−0.004	0.065	0.281	0.569
311		05/14 0223 (134) 05/14 0600	24.48	F_r	356.4	L	SN	153.	−7.	−0.005	0.046	0.291	0.842
312		06/06 0209 (157) 06/06 1423	33.62	F^+	428.3	L	SNS	106.	−46.	−0.033	0.170	0.426	0.375
313		06/27 1351 (178) 06/28 0223	33.60	F_r	391.7	L	NSS	313.	−56.	−0.023	0.145	0.209	0.893
314		07/04 1717 (185) 07/05 0405	58.32	C_x										
315		07/12 1643 (193) 07/12 2024	51.12	C_x										
316		09/01 0614 (244) 09/01 1355	12.02	F_r	486.5	L	SNS	51.	−35.	−0.093	0.108	0.256	0.323
317		10/02 0115 (275) 10/02 1535	6.00	E										
318		10/03 0000 (276) 10/03 0000	14.87	F_r	487.3	L	N	23.	37.	0.023	0.061	0.415	0.710
319		10/30 1814 (303) 10/30 1814	11.28	F_r	341.8	R	SNS	246.	−33.	−0.054	0.069	0.376	0.190
320		11/08 2107 (312) 11/08 2359	6.25	F_r	409.6	L	S	337.	−49.	0.001	0.022	0.238	0.787
321		11/23 0014 (327) 11/23 0447	10.80	F_r	356.9	R	SNS	296.	−47.	0.017	0.045	0.579	0.397
322		11/30 2023 (334) 12/01 0448	46.55	C_x										
323		12/08 0731 (342) 12/08 1647	9.37	F^-	553.1	L	SNS	70.	−33.	−0.082	0.099	0.204	0.593
324		12/14 1647 (348) 12/15 1647	12.73	F_r	460.0	R	NS	51.	−11.	0.060	0.080	0.417	0.503

Table 5 (*Continued*)

E	Year	ICME$_s$ (DOY) MO$_s$	ΔT_{MO} hrs	MO	V_{sw} kms^{-1}	H	Conf.	ϕ (°)	θ (°)	y_0 (AU)	R (AU)	χ^2	ρ
325		12/24 2036 (358) 12/25 0447	13.20	F^+	299.3	L	S	79.	−60.	0.018	0.046	0.324	0.482
326	2014	02/05 1250 (36) 02/06 0223	37.68	E									
327		02/15 1246 (46) 02/16 0043	13.68	F_r	389.2	L	N	251.	59.	−0.016	0.057	0.642	0.769
328		02/18 0559 (49) 02/18 1507	18.47	F_r	420.5	L	S	323.	−62.	−0.019	0.086	0.360	0.488
329		02/19 0309 (50) 02/19 0309	23.48	C_x									
330		04/05 0958 (95) 04/05 2218	40.10	F_r	370.1	L	S	319.	−26.	0.293	0.319	0.411	0.209
331		04/11 0657 (101) 04/11 0657	37.92	F^+	350.8	R	SNS	245.	−63.	0.007	0.153	0.226	0.683
332		04/20 1020 (110) 04/21 0741	22.53	F_r	551.7	L	SNN	75.	65.	0.009	0.138	0.651	0.596
333		04/29 1911 (119) 04/29 1911	21.37	F_r	302.8	L	S	338.	−48.	−0.053	0.080	0.261	0.628
334		06/07 1630 (158) 06/08 1912	45.58	C_x									
335		06/22 1828 (173) 06/22 1828	27.60	F^-	357.7	R	SNS	247.	−42.	−0.226	0.252	0.404	0.223
336		06/29 1647 (180) 06/29 2053	14.38	F_r	347.3	L	SNN	61.	27.	−0.025	0.055	0.468	0.698
337		07/02 2348 (183) 07/03 0307	8.88	F^-	333.5	R	S	168.	−26.	−0.124	0.125	0.318	0.058
338		08/19 0549 (231) 08/19 1759	49.18	F^+	349.1	R	NSN	55.	45.	−0.022	0.185	0.566	0.533
339		08/26 0240 (238) 08/27 0307	18.70	F_r	308.1	L	S	81.	−63.	−0.015	0.068	0.323	0.430
340		09/12 1517 (255) 09/12 2122	38.28	F^-	594.5	L	N	350.	9.	−0.154	0.167	0.449	0.037
341	2015	01/07 0538 (7) 01/07 0628	14.65	F^+	452.0	L	SN	48.	5.	−0.011	0.057	0.384	0.731
342		03/28 0336 (87) 03/28 1145	26.65	F_r	391.7	L	NSN	209.	12.	0.103	0.120	0.219	0.860
343		03/31 0732 (90) 03/31 1757	15.88	F^-	403.4	R	NS	159.	10.	−0.073	0.079	0.219	0.064
344		04/09 0909 (99) 04/09 2302	34.57	C_x									
345		05/06 0056 (126) 05/06 1648	21.58	F^-	420.7	L	SNN	156.	35.	0.028	0.073	0.280	0.584
346		05/08 0252 (128) 05/08 0711	27.38	F^-	382.8	L	SN	55.	−10.	0.279	0.298	0.185	0.565
347		05/10 0823 (130) 05/10 1159	16.80	F^+	358.2	R	NSS	140.	−33.	−0.015	0.055	0.363	0.773

Table 5 *(Continued)*

E	Year	ICME$_s$ (DOY) MO$_s$	ΔT_{MO} hrs	MO	V_{sw} km s^{-1}	H	Conf.	ϕ (°)	θ (°)	y_0 (AU)	R (AU)	χ^2	ρ
348		06/22 1807 (173) 06/23 0223	34.67	C_x									
349		09/07 1305 (250) 09/07 2331	39.35	F^+	466.3	R	NSN	46.	35.	−0.053	0.182	0.435	0.679
350		10/06 2135 (279) 10/06 2135	12.48	F_r	425.4	R	NSS	140.	−30.	0.018	0.046	0.483	−0.051
351		10/24 1759 (297) 10/25 1311	72.00	F_r	393.8	L	S	200.	−59.	−0.562	0.635	0.266	0.423
352		11/06 1746 (310) 11/07 0711	33.60	F_r	526.6	R	SNN	226.	15.	0.007	0.155	0.320	0.813
353		12/19 1535 (353) 12/20 1340	33.37	F_r	398.1	R	SNS	218.	−32.	−0.083	0.141	0.264	0.776

References

Badruddin, Mustajab, F., Derouich, M.: 2018, Geomagnetic response of interplanetary coronal mass ejections in the Earth's magnetosphere. *Planet. Space Sci.* **154**, 1. DOI. ADS.

Balmaceda, L.A., Vourlidas, A., Stenborg, G., Dal Lago, A.: 2018, How reliable are the properties of coronal mass ejections measured from a single viewpoint? *Astrophys. J.* **863**, 57. DOI. ADS.

Bothmer, V., Schwenn, R.: 1998, The structure and origin of magnetic clouds in the solar wind. *Ann. Geophys.* **16**(1), 1.

Burlaga, L., Sittler, E., Mariani, F., Schwenn, R.: 1981, Magnetic loop behind an interplanetary shock – Voyager, Helios, and IMP 8 observations. *J. Geophys. Res.* **86**, 6673. DOI. ADS.

Démoulin, P., Dasso, S., Janvier, M.: 2013, Does spacecraft trajectory strongly affect detection of magnetic clouds? *Astron. Astrophys.* **550**, A3. DOI. ADS.

Fox, N.J., Velli, M.C., Bale, S.D., Decker, R., Driesman, A., Howard, R.A., Kasper, J.C., Kinnison, J., Kusterer, M., Lario, D., Lockwood, M.K., McComas, D.J., Raouafi, N.E., Szabo, A.: 2016, The solar probe plus mission: Humanity's first visit to our star. *Space Sci. Rev.* **204**(1), 7. DOI.

Gopalswamy, N., Lara, A., Yashiro, S., Howard, R.A.: 2003, Coronal mass ejections and solar polarity reversal. *Astrophys. J. Lett.* **598**, L63. DOI. ADS.

Gopalswamy, N., Yashiro, S., Xie, H., Akiyama, S., Mäkelä, P.: 2015, Properties and geoeffectiveness of magnetic clouds during solar cycles 23 and 24. *J. Geophys. Res.* **120**, 9221. DOI. ADS.

Hidalgo, M.A., Cid, C., Vinas, A.F., Sequeiros, J.: 2002, A non-force-free approach to the topology of magnetic clouds in the solar wind. *J. Geophys. Res.* **107**, 1002. DOI. ADS.

Huttunen, K.E.J., Schwenn, R., Bothmer, V., Koskinen, H.E.J.: 2005, Properties and geoeffectiveness of magnetic clouds in the rising, maximum and early declining phases of solar cycle 23. *Ann. Geophys.* **23**, 625. DOI. ADS.

Jian, L.K., Russell, C.T., Luhmann, J.G., Galvin, A.B.: 2018, STEREO observations of interplanetary coronal mass ejections in 2007 – 2016. *Astrophys. J.* **855**, 114. DOI. ADS.

Klein, L.W., Burlaga, L.F.: 1982, Interplanetary magnetic clouds at 1 AU. *J. Geophys. Res.* **87**, 613. DOI. ADS.

Lepping, R.P., Burlaga, L.F., Jones, J.A.: 1990, Magnetic field structure of interplanetary magnetic clouds at 1 AU. *J. Geophys. Res.* **95**, 11957. DOI. ADS.

Lepping, R.P., Wu, C.-C.: 2010, Selection effects in identifying magnetic clouds and the importance of the closest approach parameter. *Ann. Geophys.* **28**, 1539. DOI. ADS.

Lepping, R.P., Wu, C.-C., Berdichevsky, D.B.: 2005, Automatic identification of magnetic clouds and cloud-like regions at 1 AU: Occurrence rate and other properties. *Ann. Geophys.* **23**, 2687. DOI. ADS.

Lepping, R.P., Wu, C.-C., Berdichevsky, D.B., Szabo, A.: 2015, Wind magnetic clouds for 2010 – 2012: Model parameter fittings, associated shock waves, and comparisons to earlier periods. *Solar Phys.* **290**, 2265. DOI. ADS.

Li, Y., Luhmann, J.G., Lynch, B.J.: 2018, Magnetic clouds: Solar Cycle dependence, sources, and geomagnetic impacts. *Solar Phys.* **293**, 135. DOI. ADS.

Li, Y., Luhmann, J.G., Lynch, B.J., Kilpua, E.K.J.: 2011, Cyclic reversal of magnetic cloud poloidal field. *Solar Phys.* **270**, 331. DOI. ADS.

Li, Y., Luhmann, J.G., Lynch, B.J., Kilpua, E.K.J.: 2014, Magnetic clouds and origins in STEREO era. *J. Geophys. Res. Space Phys.* **119**, 3237. DOI. ADS.

Low, B.C.: 2001, Coronal mass ejections, magnetic flux ropes, and solar magnetism. *J. Geophys. Res.* **106**, 25141. DOI. ADS.

Lundquist, S.: 1950, Magnetohydrostatic fields. *Ark. Fys.* **2**, 361.

Manchester, W., Kilpua, E.K.J., Liu, Y.D., Lugaz, N., Riley, P., Török, T., Vršnak, B.: 2017, The physical processes of CME/ICME evolution. *Space Sci. Rev.* **212**, 1159. DOI. ADS.

Müller, D., Marsden, R.G., St. Cyr, O.C., Gilbert, H.R.: 2013, Solar Orbiter. Exploring the Sun-Heliosphere connection. *Solar Phys.* **285**, 25. DOI. ADS.

Mulligan, T., Russell, C.T., Luhmann, J.G.: 1998, Solar cycle evolution of the structure of magnetic clouds in the inner heliosphere. *Geophys. Res. Lett.* **25**, 2959. DOI. ADS.

Nieves-Chinchilla, T.: 2018, Modeling heliospheric flux rope: A comparative analysis of physical quantities. *IEEE Transactions of Plasma Physics*.

Nieves-Chinchilla, T., Linton, M.G., Hidalgo, M.A., Vourlidas, A., Savani, N.P., Szabo, A., Farrugia, C., Yu, W.: 2016, A circular–cylindrical flux-rope analytical model for magnetic clouds. *Astrophys. J.* **823**(1), 27. DOI

Nieves-Chinchilla, T., Vourlidas, A., Raymond, J.C., Linton, M.G., Al-haddad, N., Savani, N.P., Szabo, A., Hidalgo, M.A.: 2018, Understanding the internal magnetic field configurations of ICMEs using more than 20 years of *Wind* observations. *Solar Phys.* **293**(2), 25. DOI.

Palmerio, E., Kilpua, E.K.J., Möstl, C., Bothmer, V., James, A.W., Green, L.M., Isavnin, A., Davies, J.A., Harrison, R.A.: 2018, Coronal magnetic structure of Earthbound CMEs and in situ comparison. *ArXiv e-prints*. ADS.

Richardson, I.G., Cane, H.V.: 2004, Identification of interplanetary coronal mass ejections at 1 AU using multiple solar wind plasma composition anomalies. *J. Geophys. Res. Space Phys.* **109**, A09104. DOI. ADS.

Riley, P., Richardson, I.G.: 2013, Using statistical multivariable models to understand the relationship between interplanetary coronal mass ejecta and magnetic flux ropes. *Solar Phys.* **284**, 217. DOI. ADS.

Vourlidas, A.: 2014, The flux rope nature of coronal mass ejections. *Plasma Phys. Control. Fusion* **56**(6), 064001. DOI. ADS.

Vourlidas, A., Webb, D.F.: 2018, Streamer-blowout coronal mass ejections: Their properties and relation to the coronal magnetic field structure. *Astrophys. J.* **861**(2), 103. DOI.

Vourlidas, A., Howard, R.A., Esfandiari, E., Patsourakos, S., Yashiro, S., Michalek, G.: 2010, Comprehensive analysis of coronal mass ejection mass and energy properties over a full solar cycle. *Astrophys. J.* **722**(2), 1522. DOI.

Vourlidas, A., Balmaceda, L.A., Stenborg, G., Dal Lago, A.: 2017, Multi-viewpoint coronal mass ejection catalog based on STEREO COR2 observations. *Astrophys. J.* **838**, 141. DOI. ADS.

Wu, C.-C., Lepping, R.P.: 2015, Comparisons of characteristics of magnetic clouds and cloud-like structures during 1995 – 2012. *Solar Phys.* **290**, 1243. DOI. ADS.

Yashiro, S., Gopalswamy, N., Michalek, G., St. Cyr, O.C., Plunkett, S.P., Rich, N.B., Howard, R.A.: 2004, A catalog of white light coronal mass ejections observed by the SOHO spacecraft. *J. Geophys. Res. Space Phys.* **109**, A07105. DOI. ADS.